

ORIGINAL RESEARCH

Open Access



N self-doped multifunctional chitosan biochar-based microsphere with heterogeneous interfaces for self-powered supercapacitors to drive overall water splitting

Chunxia Yan¹, Yaqi Yang¹, Jie Wei¹, Jianhua Hou² and Ziqiang Shao^{1*} 

Abstract

Due to the rising need for clean and renewable energy, green materials including biochar are becoming increasingly popular in the field of energy storage and conversion. However, the lack of highly active and stable electrode materials hinders the development of stable energy supplies and efficient hydrogen production devices. Herein, we fabricated stable, conductive, and multifunctional chitosan microspheres by a facile emulsion crosslinking solution growth and hydrothermal sulphuration methods as multifunctional electrodes for overall water splitting driven by supercapacitors. This material possessed three-dimensional layered conductors with favorable heterojunction interface, ample hollow and porous structures. It presented remarkably enhanced electrochemical and catalytic activity for both supercapacitors and overall water electrolysis. The asymmetric supercapacitors based on chitosan biochar microsphere achieved high specific capacitance (260.9 F g^{-1} at 1 A g^{-1}) and high energy density (81.5 W h kg^{-1}) at a power density of 978.4 W kg^{-1} . The chitosan biochar microsphere as an electrode for electrolyze only required a low cell voltage of 1.49 V to reach a current density of 10 mA cm^{-2} , and achieved excellent stability with 30 h continuous test at 20 mA cm^{-2} . Then, we assembled a coupled energy storage device and hydrogen production system, the SCs as a backup power source available guaranteed the continuous operation of overall water electrolysis. Our study provides valuable perspectives into the practical design of both integrated biochar-based electrode materials and coupled energy storage devices with energy conversion and storage in practical.

Highlights

- A highly conductive and multifunctional chitosan-based microsphere was fabricated.
- Chitosan-based microsphere possessed favorable heterojunction interface.
- This electrode presented remarkable electrochemical and catalytic activity.
- The ASCs delivered remarkable energy density and power density.
- A coupled energy storage device and hydrogen production system was established.

Keywords Chitosan microsphere, Biochar, Heterojunction interface, Multifunctional electrode, Coupled energy storage device

Handling editor: Kitae Baek

*Correspondence:

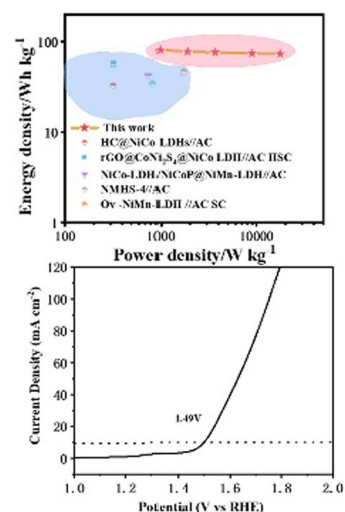
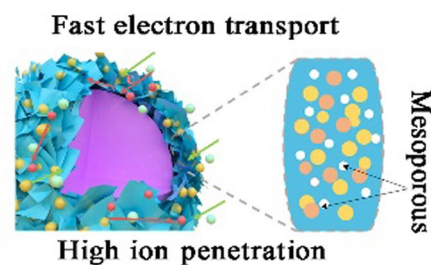
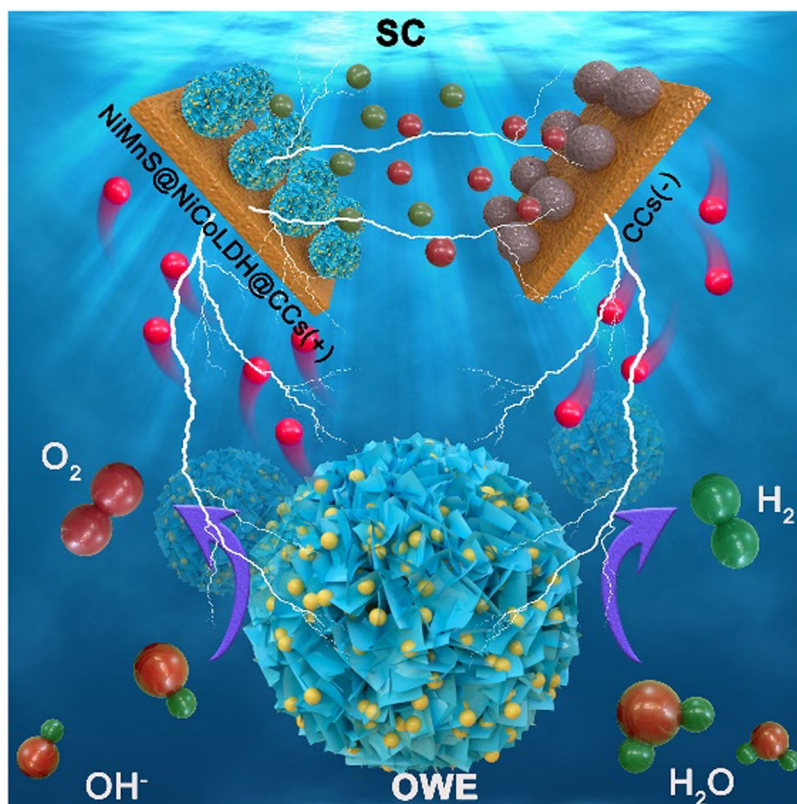
Ziqiang Shao
shaoziqiang@263.net

Full list of author information is available at the end of the article



© The Author(s) 2023. **Open Access** This article is licensed under a Creative Commons Attribution 4.0 International License, which permits use, sharing, adaptation, distribution and reproduction in any medium or format, as long as you give appropriate credit to the original author(s) and the source, provide a link to the Creative Commons licence, and indicate if changes were made. The images or other third party material in this article are included in the article's Creative Commons licence, unless indicated otherwise in a credit line to the material. If material is not included in the article's Creative Commons licence and your intended use is not permitted by statutory regulation or exceeds the permitted use, you will need to obtain permission directly from the copyright holder. To view a copy of this licence, visit <http://creativecommons.org/licenses/by/4.0/>.

Graphical Abstract



1 Introduction

With growing concern about energy usage and growing need for environmentally friendly energy, improved green energy conversion and storage technologies, particularly overall water electrolysis (overall water electrolysis) (Du et al. 2019; You and Sun 2018; You et al. 2019) and supercapacitors (SCs) (Choudhary et al. 2017; Zhu et al. 2019b), have captured extensive investigation of researchers worldwide. In the sphere of energy conversion, one of the most often used hydrogen production technologies is electrocatalytic extraction of hydrogen from water (Han et al. 2021; Sun et al. 2020). Besides, overall water electrolysis can achieve zero greenhouse gas emissions and high calorific value (Wu et al. 2020). The electric energy sources of overall water electrolysis system mainly derive from power grid and renewable energy. However, the widespread use of overall water electrolysis technology is hampered by the high price of electricity, and renewable energy sources, which include mainly wind power and solar cells, are intermittent and unstable depending on the climatic environment (Ayodele and Munda 2019; Zhu et al. 2022). These factors will

reduce stability and service life of the electrolytic cell. Therefore, it is urgent to design a coupled energy storage device and hydrogen production facility to guarantee high productivity and stability of the overall water electrolysis system, as well as high energy utilization rate. SCs with superior energy density, fast charging/discharging rates and outstanding cycle performance are highly competitive in the energy storage market. It is principally applied in rail transit, renewable energy (Libich et al. 2018), power systems (Zhang et al. 2016). What is noticeable is that SCs as micro-grid energy buffer units, provide standby capacity not only to ensure the normal operation of the system and but also enhance system reliability (Song et al. 2016). However, SCs suffer from low energy density and poor conductivity. Moreover, the catalyst for overall water electrolysis also faces the same issue about poor activity and stability. To date, the most common overall water electrolysis catalysts are precious metals-based materials, specifically Pt (Li et al. 2021b), Ir (Luo et al. 2020) and Ru (Lin et al. 2021). Unfortunately, the commercial applicability of these electrocatalysts is limited due to their high price and short lifespan.

Consequently, hunt for effective, robust, and precious-metal-free electrocatalysts has aroused great interest in overall water electrolysis. Furthermore, bifunctional electrocatalysts (Fan et al. 2018; Wang et al. 2021b) can achieve both oxygen evolution reaction (OER) and hydrogen evolution reaction (HER), meanwhile simplify the overall water electrolysis equipment. Therefore, it is essential to rationally construct an innovative and affordable multifunctional electrode material for SCs as well as overall water electrolysis (HER and OER).

Biochar-based materials are proved to be a rational substitute for noble metal materials in energy storage and energy conversion (Borenstein et al. 2017; Li et al. 2021a). Biochar-based materials, including activated carbon (Sun et al. 2016), graphene (Tan and Lee 2013), carbon nanotubes (Toma et al. 2011), and various biochar (Zhou et al. 2019) have been thoroughly used for SCs and overall water electrolysis. The most prominent of these is biochar, which not only has low cost and environmental friendliness, but also has self-doped effect during pyrolysis (Wang et al. 2021a). It is noteworthy that chitosan widely exists in crab shells and shrimp shells (Aswathy et al. 2020; Roy et al. 2021). Considering that chitosan contains plentiful nitrogen heteroatoms, it is a valuable biomass raw material for biochar synthesis. However, insufficient electroactive sites, low energy density and poor electrochemical reaction kinetics of biomass carbon materials make their electrochemical performance far inferior to practical industrial requirements. Therefore, improving the electrochemical activity of biochar from both structural and material aspects is a valuable method. In terms of structure, interface engineering has been used to adjust the electronic structure and form active interface. Establishing heterojunctions between different functional components availably changes the electronic configuration of nanointerfaces, adjusts the electronic state of active sites, drastically reduces energy barriers, and thus efficiently accelerates charge transfer capability and electrochemical reaction kinetics (Kuang et al. 2017; Ong and Shak 2020; Yu et al. 2021). Layered double hydroxides (LDHs) derived from metal–organic framework (MOF) not only reserve the advantages of self-assembled framework structure of MOF, uniform distribution of intrinsic metal and abundant nanopores/channels, but also possess unique layered structure, large specific surface area and high redox activity, which can simultaneously realize charge storage and transfer (Abd El-Monaem et al. 2023; Eltaweil et al. 2023; Li et al. 2019a; Omer et al. 2023; Wang et al. 2021c; Yilmaz et al. 2017). So LDHs have received extensive attention. Nevertheless, agglomeration and recombination of 2D LDH nanosheets, inherently low conductivity and simplex little pore size severely restrain charge transfer, resulting in

poor electrochemical performance. Notably, the phase and structure of metal compounds are transformed into metal sulfides by post-treatments for the original MOFs, so that higher catalytic activity and more exposed active sites can be obtained (He et al. 2018; Shi et al. 2022). In addition, bimetallic sulfides have a synergistic effect of bimetal (Huang et al. 2016; Tang et al. 2018; Xin et al. 2017). Moreover, due to the electronic modulation of doped metal, the *OH potential barrier is immensely reduced and the reaction kinetics is highly accelerated. Interestingly, it exhibits the dual functional properties to achieve both HER and OER in overall water electrolysis as well as SCs applications. As far as we know, although these heterostructures and multiphase materials are making encouraging development, their electrochemical activity has not yet achieved applied standard. Therefore, in order to simultaneously apply to SCs and overall water electrolysis, a type of multifunctional heterostructure material with high electrochemical reactivity and high stability is urgently needed.

In this work, we successfully designed a multifunctional chitosan biochar microsphere with a tunable 3D heterostructure, which can be used as a multifunctional electrode for overall water splitting driven by supercapacitors. The ample polymetallic heterojunctions for NiMnS/NiCo LDH, hollow and various types of porous structures expose more active sites and abundant ion/electron channels, which facilitate electrochemical activity. The material has the potential to be used to create SCs with efficient charge storage, as well as electrodes for the hydrogen evolution process (HER) and oxygen evolution reaction (OER). Therefore, a coupled energy storage device and hydrogen production system based on this electrode material to fulfill the demands of industries was designed. SCs with high energy density ensure the efficient and stable operation of the overall water electrolysis. Moreover, the smooth and stable progress for overall water electrolysis can be achieved without manipulating the main power sources and under conditions of changing external environment. This work provides a platform for the design of integrated electrode materials for efficient and stable energy conversion and storage. The results help design efficient coupled energy storage devices and hydrogen production systems.

2 Experimental section

2.1 Synthesis of chitosan

Chitosan was prepared according to previous literature. The lobster shells were demineralized in 1 L 1 M HCl, and rinsed with distilled water until the PH value was neutral. The demineralized shell was treated with 1 M NaOH for 3 h at 80 °C to produce chitin. The chitosan is produced by deacetylating in 12.5 M NaOH.

Relevant characterizations are listed in the supporting information.

2.2 Synthesis of chitosan biochar microspheres

Chitosan microspheres (Cs) were created by the emulsion crosslinking. Chitosan dissolved in 2% acetic acid to form aqueous phase. The oil phase consisted of 190 mL liquid paraffin and 10 mL Span-80. The aqueous phase was added to the oil phase under agitation to form an emulsion. Subsequently, 25% glutaraldehyde was added as a crosslinking agent. The mixture was heated at 40 °C for 2 h and 70 °C for 2 h. Finally, the Cs was obtained by washing with petroleum ether, acetone, and ethanol.

Then, the Cs was carbonated at 700 °C, 800 °C, 900 °C for 2 h in N₂ to obtain the conductive and carbonated Cs (CCs), as well as biochar microspheres. The obtained CCs were labeled CCs-700, CCs-800, and CCs-900, respectively.

2.3 Synthesis of NiCoLDH@CCs

A certain concentration of Co (NO₃)₂·6H₂O and Ni (NO₃)₂·6H₂O were dissolved in methanol. Then, the prepared CCs were immersed in the abovementioned solutions. 2-dimethylimidazole was added to the solutions for co-deposition for 12 h to obtain NiCoLDH@CCs. The Ni²⁺/Co²⁺ concentration was varied as 0.1, 0.3, and 0.5, and the obtained systems were labeled NiCoLDH-0.1@CCs, NiCoLDH-0.3@CCs, and NiCoLDH-0.5@CCs, respectively.

2.4 Synthesis of NiMnS@NiCoLDH@CCs

The 1:1:3 of Ni (NO₃)₂·6H₂O, MnCl₂·6H₂O, and thioacetamide were dissolved in distilled water. NiMnS@NiCoLDH@CCs were produced by hydrothermal heating at 120 °C for 2 h. The concentration of the sodium thiosulfate solution was varied as 0.1, 0.3, and 0.5 to regulate the degree of vulcanization. The obtained materials were labeled NiMnS1@NiCoLDH@CCs, NiMnS2@NiCoLDH@CCs, and NiMnS3@NiCoLDH@CCs, respectively. For comparison, we also prepared NiMnS by hydrothermal reaction.

3 Results and discussion

3.1 Preparation and characterization of NiMnS @ NiCoLDH@CCs

The fabrication of NiMnS @NiCoLDH@CCs is schematically depicted in Fig. 1a. First, Cs microspheres with a diameter of about 4–5 μm were generated by facile emulsion crosslinking method using chitosan obtained from the treated crab shells (Additional file 1: Fig. S1). The surface of the generated Cs microspheres was smooth. FTIR (Additional file 1: Fig. S2a) showed that

glutaraldehyde crosslinked chitosan microspheres added an aliphatic C–H stretching vibration signature at 2923 cm⁻¹ as compared to pristine chitosan. And C–H deformations responsible for two absorption bands at 2851 and 1378 cm⁻¹ was found in microsphere spectra. Moreover, some signatures in the Cs spheres curve were also missing, including N–H belonging to amide II bands (~1596 cm⁻¹), C–O asymmetric stretching vibration (~1154 cm⁻¹), and glycosidic bond vibration ranging from ~895 to ~661 cm⁻¹, further explaining the formation of Cs microspheres. After high-temperature carbonization, the Cs microsphere transformed into highly conductive graphitic biochar microspheres with rich N elements. The smooth surfaces of the carbonized Cs (CCs) became rough (Fig. 1b1–b3), contributing to the adsorption of other substances. Then, Ni/Co LDHs nanosheets with an average thickness of approximately 40 nm were evenly dispersed on the CCs substrate by the solution growth method (Fig. 1c1, 1c2). Concurrently, numerous open pore structures about 100–200 nm were formed by interlacing between 50 nm thick Ni/Co nanosheets with smooth surfaces (Fig. 1c3). After sulfidation and etching, the primary smooth surface of Ni/Co LDHs became rough and produced abundant hollow and porous structure (Fig. 1d). Plentiful NiMnS spheres anchored in the surface of Ni/Co nanosheets, constituting heterojunction structure.

3.2 Morphology and structure characterization

TEM was performed to investigate surface structures and interfaces of the NiCoLDH@CCs and NiMnS @NiCoLDH@CCs. In contrast to the CCs microspheres (Additional file 1: Fig. S1b), the NiCoLDH@CCs was uniformly covered with well-ordered 3D interconnected Ni/Co LDH shell about 430 nm thick (Fig. 2a, b), which is consistent with the SEM analysis (Fig. 1c). According to HRTEM analysis in Fig. 2c, there were clearly heterointerfaces between CCs and Ni/Co LDH. The lattice fringes were 0.22 nm, belonging to the (101) planes of CN_x (blue label). Additionally, the lattice fringes of 0.21 and 0.23 nm were corresponded to the (103) and (002) planes of Ni (OH)₂ (gray label) and Co (OH)₂ (pink label) for Ni/Co LDHs, respectively. The corresponding selected area electronic diffraction pattern (SAED) in Fig. 2d shows that NiCoLDH@CCs was polycrystalline. The EDS elemental mappings (Additional file 1: Fig. S3) indicated that the even-distributed Ni, Co elements C, N, O, manifesting the formation of NiCoLDH@CCs. TEM (Fig. 2e, F) showed that the external Ni/Co LDHs nanosheets after sulfidation treatment transformed into NiCoS, and the layered morphology was perfectly reserved with a thickness of 450 nm, which basically bring into correspondence with that of NiCoLDH@CCs. Specially, a typical

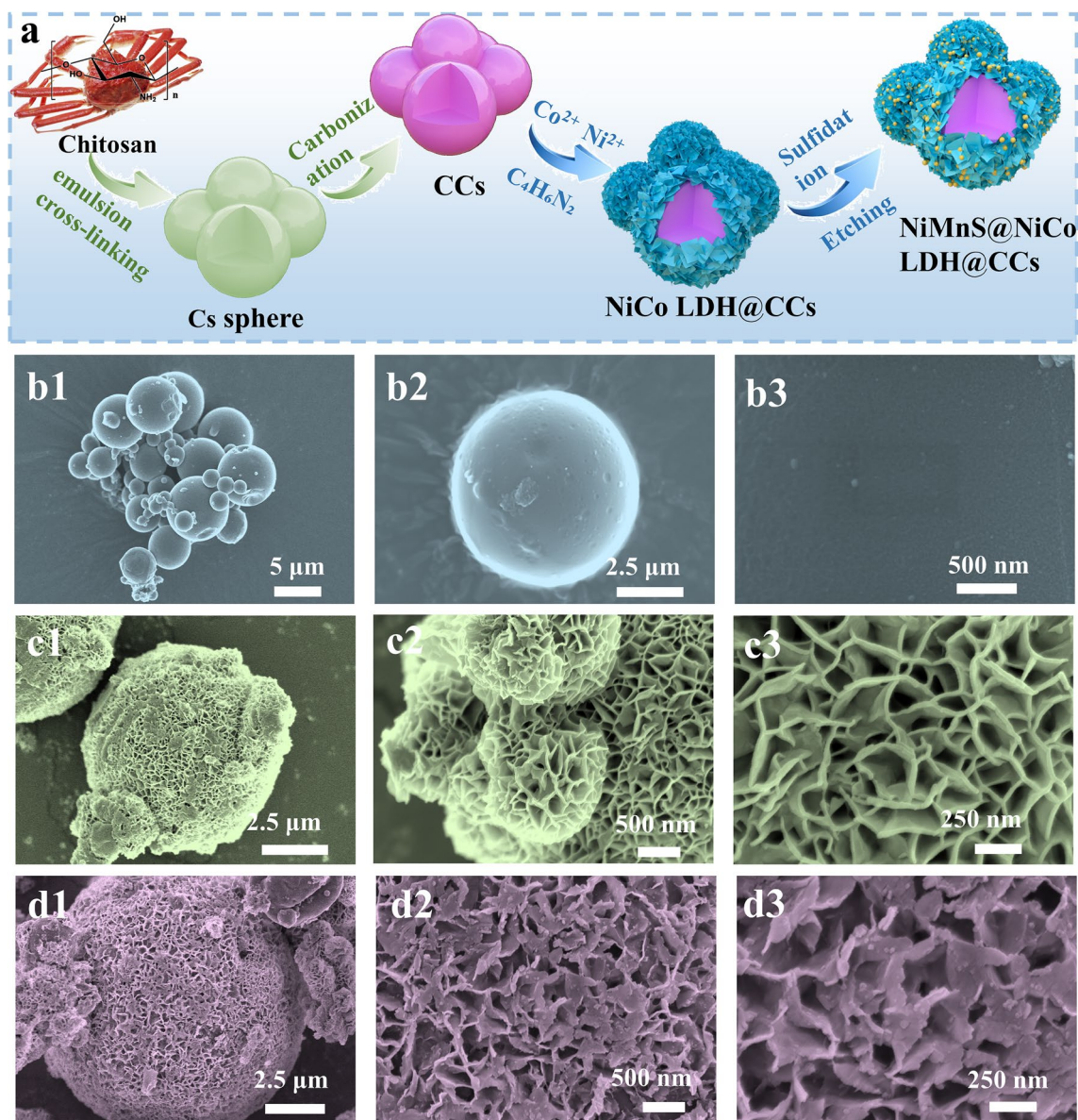


Fig. 1 a Schematic diagram of NiMnS@NiCoLDH@CCs electrode manufacturing process. SEM images of (b1–b3) CCs, (c1–c3) NiCoLDH@CCs (d1–d3) NiMnS@NiCoLDH@CCs at different magnifications

hollow structure and ample nanoporous on the surface of Ni/Co LDHs was obtained after etching by Ni^{2+} and Mn^{2+} (Fig. 2f), contributing to the fast electrolyte diffusion and the more accessible electrochemical active sites. Notably, Fig. 2f suggests that vast NiMnS nanoparticles covered on the surface of Ni/Co LDHs. The HRTEM (Fig. 2g) revealed that there obviously existed several heterointerfaces between Ni/Co LDHs and NiMnS. The lattice fringes of 0.18 and 0.21 nm (Fig. 2g) belong to the (220) and (150) planes of MnS (yellow label) and Ni_9S_8 (cyan label), respectively. While the interlayer spacings of

0.19 nm are ascribed to the (331) plane of NiCoS_4 . Concurrently, apparent lattice fringe dislocation and deformation, as well as lattice fringe fracture were observed (Additional file 1: Fig. S4), due to absence of atoms, further uncovering the existence of abundant defects. The ample defects and disordered area at the interface offer extra and virous active sites to promote charge transfer and enhance HER/OER reactivity (Zhu et al. 2019a). Besides, the SAED (Fig. 2h) further improved that NiMnS@NiCoLDH@CCs had polycrystalline phase. The EDS (Fig. 2i) indicated the homogenous distribution of

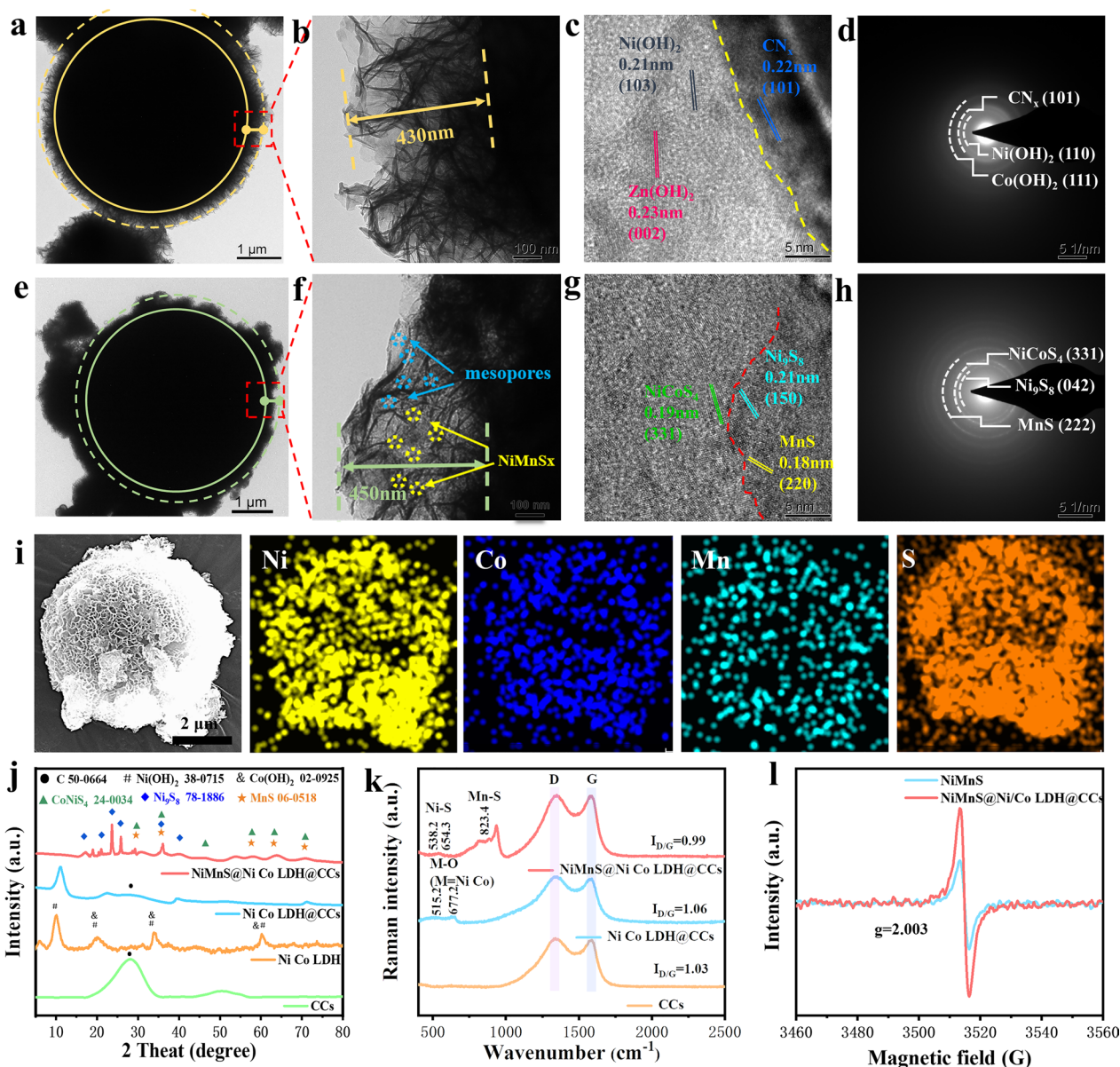


Fig. 2 **a, b** TEM images of NiCoLDH@CCs at diverse magnifications. **c** HRTEM image **d** SAED image of NiCoLDH@CCs. **e, f** TEM images of NiMnS@NiCoLDH@CCs at different magnifications. **g** HRTEM image **h** SAED image of NiMnS@NiCoLDH@CCs. **i** EDS of NiMnS@NiCoLDH@CCs. **j** XRD patterns **k** Raman spectroscopy of CCs, NiCoLDH@CCs, NiMnS@NiCoLDH@CCs, respectively. **l** electron paramagnetic resonance (EPR) spectra of NiMnS and NiMnS@NiCoLDH@CCs, respectively

the Ni, Co, Mn, and S elements in NiMnS@NiCoLDH@CCs. The above findings confirm that the NiMnS@NiCoLDH@CCs can be successfully heterostructured with hollow and porous structure. Additional file 1: Figs. S5a–d show that the Ni/Co LDH nanosheets on CCs gradually grew and formed nanoflowers along with rise of the concentration of Ni²⁺/Co²⁺ (Additional file 1: Fig. S5c). Besides, nanoflowers extremely agglomerated in higher concentration and greatly lengthens the distance

for electrolyte ion diffusion, which is detrimental to charge/discharge migration and electrochemical kinetics. The optimum Ni²⁺/Co²⁺ concentration was 0.3 mM. We further explored the influence of vulcanization degree on the structure of NiMnS@NiCoLDH@CCs. As depicted in Additional file 1: Fig. S6a–c, with the increase of the vulcanization degree, the lamellar structure of NiCoLDH gradually collapsed, finally it was tightly wrapped by

NiMnS and the nanochannel disappeared, which was not conducive to ion migration and electron transmission.

The phases and crystallinity were detected by XRD analysis. As depicted in Additional file 1: Fig. S7a, Cs sphere after carbonation shows large peak package at about 22° belonging to (002) plane of graphitic carbon (JCPDS 50-0664). It indicates the formation of conductive biocarbon sphere. Additional file 1: Fig. S7b depicts a series of diffraction peaks of MnS (JCPDS 06-0518), Ni_9S_8 (JCPDS 78-1886) and CN_x (JCPDS 50-0664), which are well matched well with NiMnS@NiCoLDH@CCs, further proving that NiMnS was synthesized after the hydrothermal process. In contrast to NiCoLDH@CCs, the characteristic peak of NiCoS_4 in NiMnS@NiCoLDH@CCs is found, indicating that Ni(OH)₂ (JCPDS 38-0715) and Co(OH)₂ (JCPDS 02-0925) precursors had been partially sulfated to bimetallic sulfides. The above results demonstrate that the synthesis of NiMnS@NiCoLDH@CCs was effective, as well as the presence of abundant heterojunction interfaces, consistent with HRTEM examination (Fig. 2j).

Raman spectra were further used to characterize the chemical structure. Figure 2k shows the characteristic peaks of metal-O (Ni/Co-O) in NiCoLDH@CCs at 515.2 and 677.2 cm^{-1} , indicating the existence of layered Ni(OH)₂ and Co(OH)₂. While for NiMnS@NiCoLDH@CCs, the peak at about 654.3 cm^{-1} and 823.4 cm^{-1} is attributed to the Mn-S/Mn-S-C vibration and the interaction of the MnS cluster with the negatively charged backbone (Avril et al. 2013; Hu et al. 2017), indicating the presence of MnS. Besides, the peak at 538.2 cm^{-1} belongs to Ni-S vibration, which shifts to a higher value in comparison to the literature (Rathore et al. 2022) due to the strong interaction between Ni-S and Mn^{2+} . The other two peaks (1350 and 1580 cm^{-1}) are the characteristics of D and G bands of carbonaceous materials (Huang et al. 2017). The I_D/I_G of CCs, NiCoLDH@CCs and NiMnS@NiCoLDH@CCs is 1.03, 1.06 and 0.99, respectively, suggesting a high degree of graphitization.

Further, FTIR measurement (Additional file 1: Fig. S2b) was conducted to investigate the chemical identities. The wide characteristic peak ranging from 3462 to 3354 cm^{-1} is O-H stretching vibration. Compared with other curves, newly observed peaks at 1097 cm^{-1} , 942 cm^{-1} , 745 cm^{-1} for NiMnS@NiCoLDH@CCs belong to in the characteristic peaks from MnS, which are similar to the reported values (Hu et al. 2017). Importantly, the metal-O (Ni/Co/Zn-O) peaks at 630 cm^{-1} . Above results suggest the successful preparation of the NiMnS@NiCoLDH@CCs.

Additionally, to further confirm the existence of sulfur defects in NiMnS@NiCoLDH@CCs, electron paramagnetic resonance (EPR) spectroscopy was utilized.

Figure 2l displays all samples have resonance signal at $g=2.003$, belonging to sulfur vacancy (Lu et al. 2018). The strength and width of sulfur vacancies in NiMnS@NiCoLDH@CCs are obviously greater than those of NiMnS, indicating more sulfur vacancies, agreeing with TEM results (Additional file 1: Fig. S4). The presence of S-vacancy changes the surface charge distribution of metal sulfide to form an electron-deficient center, which improves the electron density near the metal position. As a result, S-vacancy encourages the adsorption of significant intermediates, improving the movement of electrons and raising the catalytic performance of materials (Gong et al. 2020). Therefore, NiMnS@NiCoLDH@CCs has the highest catalytic activity.

Moreover, the BET (Additional file 1: Fig. S8a) showed specific surface area of NiMnS@NiCoLDH@CCs was 328.7 $\text{m}^2 \text{g}^{-1}$, higher than NiCoLDH@CCs (328.7 $\text{m}^2 \text{g}^{-1}$), and CCs (32.4 $\text{m}^2 \text{g}^{-1}$). It displays that the interlaced LDH nanochannels, hollow and porous LDH further increases substantially the specific surface area. Besides, a plentiful porous structure with mesopores and micropores was further demonstrated by the matching pore size distribution of NiMnS@NiCoLDH@CCs (Additional file 1: Fig. S8b), which shows a prominent peak at about 2.3 nm. In addition to exposing innumerable active sites and accelerating reaction kinetics, it aids electrolyte ions transportation and electron transformation.

The XPS analysis corroborated the oxidation state and composition. The full XPS spectrum (Fig. 3a) depicts common coexistence of Mn, Ni, Co, S, N, O and C in the NiMnS@NiCoLDH@CCs, and Additional file 1: Table S1 shows the atomic percentage of those elements, which agrees with the EDS results. The N element partly derives from the CCs, and incompletely vulcanized NO_3^- in Ni/Co LDH. The O element mostly exists in the superficial organic matter and incompletely vulcanized Ni/Co LDH. The Mn, Ni, Co and S elements originate from NiMnS@NiCoLDH@CCs electrode materials. The dominant electron state of Mn 2p was intensively identified and clearly separated into Mn 2p_{1/2} and Mn 2p_{3/2} with binding energies of about 654.8 and 642.4 eV (Fig. 3b), respectively, proving the emergence of Mn^{2+} (Zhu et al. 2020), and further indicating the presence of MnS. The peaks at 857.2 eV in Ni 2p_{3/2} and 879.2 eV in Ni 2p_{1/2} are appointed to the spin-orbit characteristics of Ni^{2+} , and the peaks at about 853.6 eV in Ni 2p_{3/2} and 875.1 eV in Ni 2p_{1/2} reckon with the characteristics of Ni^{3+} in the Ni 2p spectrum for NiMnS@NiCoLDH@CCs (Fig. 3b). (Rathore et al. 2022). Interestingly, compared with NiCoLDH@CCs, the Ni 2p_{1/2} and Ni 2p_{3/2} peaks for NiMnS@NiCoLDH@CCs slightly shift to higher binding energies, possibly due to strong bonding between NiMnS core and Ni/Co LDH shell. Importantly, it reveals that there is electronic

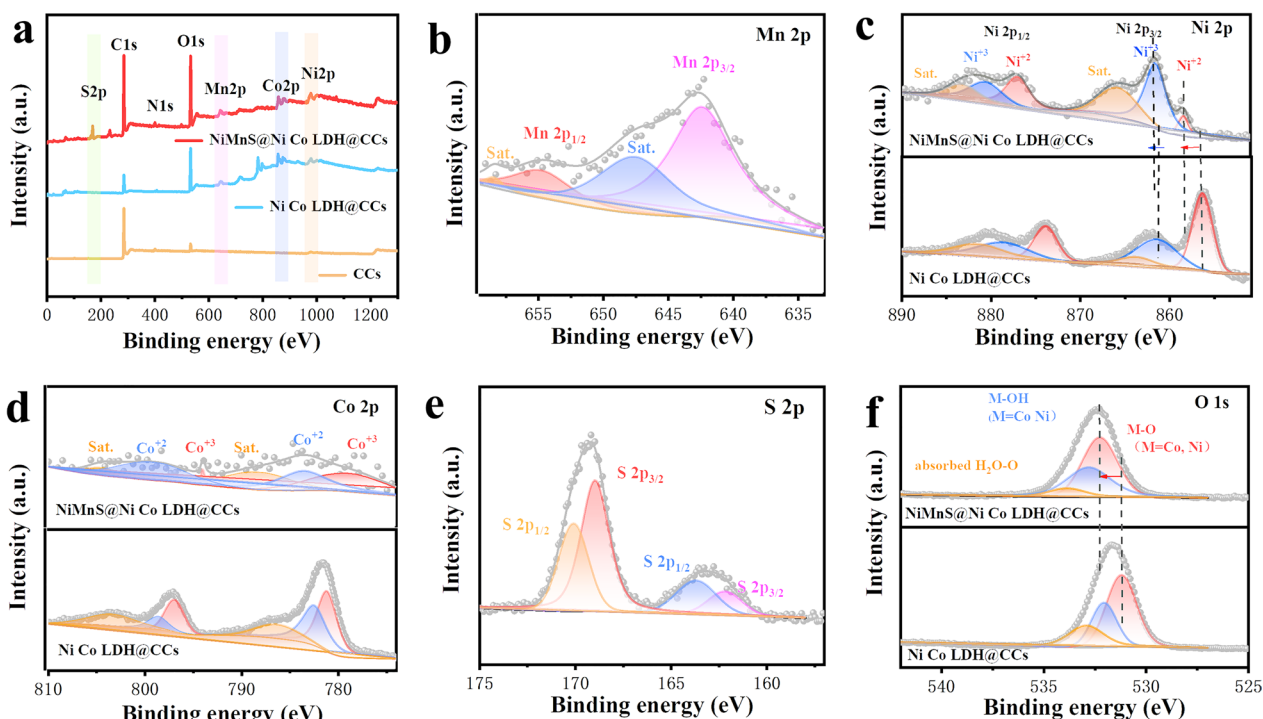


Fig. 3 a XPS of the NiMnS@NiCoLDH@CCs samples. High-resolution XPS of **b** Mn 2p, **c** Ni 2p, **d** Co 2p, **e** S 2p, and **f** O 1s. (Sat. means shake-up satellites)

coupled and electron transfer between NiMnS and Ni/Co LDH, and the heterogeneous interface is successfully constructed. Additionally, the $\text{Ni}^{3+}/\text{Ni}^{2+}$ ratio was calculated according to the XPS peak area (Additional file 1: Fig. S9). The $\text{Ni}^{3+}/\text{Ni}^{2+}$ ratio in NiMnS@NiCoLDH@CCs was extremely higher than that of NiCoLDH@CCs, indicating that the construction of heterogeneous interface could induce the increase in the proportion of oxidation state Ni^{3+} . It has been reported that Ni^{3+} exhibits higher electron affinity than Ni^{2+} due to more valence electron three-dimensional orbitals. Therefore, it has better absorption capacity for oxygen-containing intermediates generated by OER reaction, which is conducive to promote high electrocatalytic activity (Shi et al. 2019; Zhao et al. 2019). Similarly, the Co 2p XPS fitting profile (Fig. 3d) for NiMnS@NiCoLDH@CCs shows that the Co^{2+} peak is located between 782.8 and 798.7 eV, whereas the Co^{3+} peak is located between 781.4 and 793.5 eV (Kang et al. 2022). Two distinct metal sulfide and sulfate peaks are seen in the S 2p spectra (Fig. 3e). The peaks at 162.1 and 163.3 eV correspond to the S 2p_{3/2} and S 2p_{1/2} of S^{2-} , respectively.

The sulfur oxides are also indicated by the peaks at 168.9 and 170.0 eV (Kang et al. 2022). It demonstrates the existence of metal sulfides, including Ni_9S_8 , MnS and NiCoS_4 , which were found after the vulcanization

reaction of NiCoLDH@CCs. Additionally, in comparison to the NiCoLDH@CCs sample (Fig. 3c, d), the binding energies of $\text{Ni}^{2+}/\text{Ni}^{3+}$ and $\text{Co}^{2+}/\text{Co}^{3+}$ in NiMnS@NiCoLDH@CCs are positively shifted. It illustrates the NiCoS₄, Ni₉S₈, and MnS heterointerfaces have an intense electric connection that contributes to faster charging transfers and improved reaction kinetics. In the O 1s XPS spectrum (Fig. 3f), the peaks at 532.3, 532.8, and 533.9 eV are well ascribed to the metal–O, metal–OH group and adsorbed H₂O, respectively (Si et al. 2020). Besides, the M–O peak of NiMnS@NiCoLDH@CCs moves to higher peak compared to that of NiCoLDH@CCs, confirming stronger bonding of Ni/Co LDH and NiMnS.

3.3 Electrochemical performance

The electrochemical behavior of CCs-based electrodes was tested in a three-electrode system in 3 M KOH electrolyte via CV, EIS, GCD texts. The electrochemical characteristics of conductive biochar are affected by the carbonization temperature. Fig. S10 shows that CV presents a typical rectangle due to double layer capacitance. Besides, The CCs-800 electrode has a larger CV integral area than that of CCs-700 and CCs-900 electrode, indicating distinguished electrochemical performance and larger specific capacity. Figure 4a presents

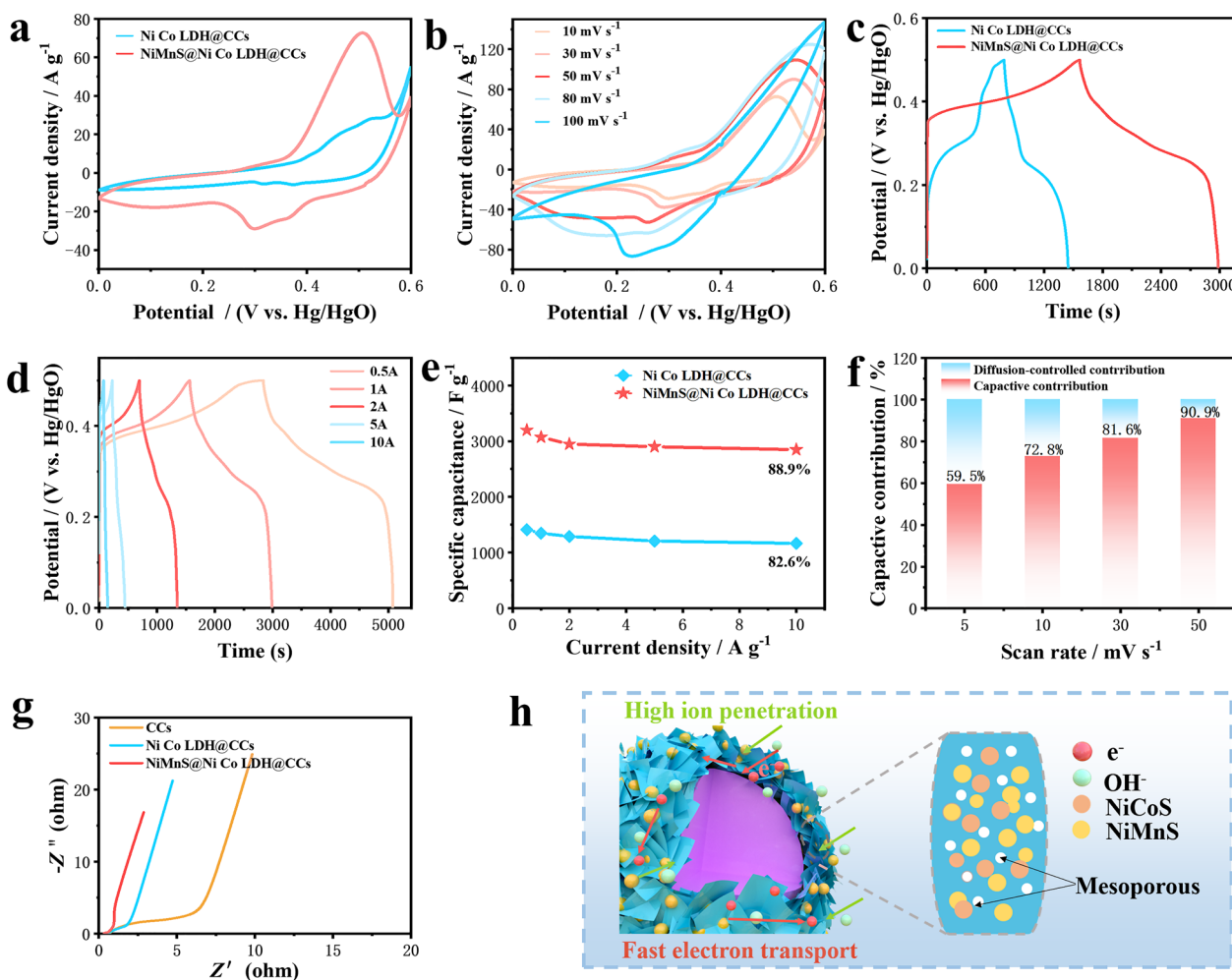


Fig. 4 **a** CV of the NiCoLDH@CCs, NiMnS@NiCoLDH@CCs sample electrodes scanned at 50 mV/s. **b** CV of the NiMnS@NiCoLDH@CCs electrode at different scanning rates. **c** GCD of the NiCoLDH@CCs, NiMnS@NiCoLDH@CCs at 1 A g⁻¹. **d** GCD of the NiMnS@NiCoLDH@CCs electrodes at different current densities. **e** The specific capacitance of NiCoLDH@CCs, NiMnS@NiCoLDH@CCs samples at various current densities. **f** Comparison of capacitive-controlled contribution of NiMnS@NiCoLDH@CCs at various scan rates. **g** Nyquist plot of NiMnS@NiCoLDH@CCs samples electrode. **h** The charge storage mechanism of the NiMnS@NiCoLDH@CCs

a couple of typical and reversible redox peaks for all CV curves at 50 mV s⁻¹ at 0–0.6 V, in accordance with reversible Faradic redox reaction and pseudocapacitance characteristics. The NiMnS@NiCoLDH@CCs electrode has a larger CV integral area than the NiCoLDH@CCs electrode, indicating distinguished pseudocapacitive properties and larger specific capacity. The redox peaks of all CV curves only slightly shift (Fig. 4b), but the shape of CV curves is well kept with rising of the scan rate ranging from 10 to 100 mV s⁻¹, indicating better reversibility. The conventional and symmetric galvanostatic charge–discharge (GCD) curves at 1 A g⁻¹ are shown in Fig. 4c. The NiMnS@NiCoLDH@CCs electrode's discharge duration is obviously longer than that of NiCoLDH@CCs electrodes,

further attesting its highest specific capacitance, which agrees with CV results. Further, GCD curve of NiMnS@NiCoLDH@CCs still maintains good symmetry with varied current densities ranging from 0.5 to 10 A g⁻¹ (Fig. 4d), suggesting high coulombic efficiency. Such wonderful symmetry and unique platform, as well as small IR drop illustrate high reversibility and high coulomb efficiency of NiMnS@NiCoLDH@CCs. The specific capacitances of NiCoLDH@CCs and NiMnS@NiCoLDH@CCs are estimated and plotted in Fig. 4e. Evidently, NiMnS@NiCoLDH@CCs (3072.6 F g⁻¹) surpasses NiCoLDH@CCs (1409.2 F g⁻¹) at 1 A g⁻¹. Even, the NiMnS@NiCoLDH@CCs electrode still retains about 88.9%, surpassing that of NiCoLDH@CCs (82.6%), which indicates prominent rate capability.

Besides, those specific capacities even greatly exceed the identical sort of reported electrode materials (Additional file 1: Table S3), such as Ov-NiMn-LDH (Tang et al. 2020), NiMn-LDH/ MXene (Zhang et al. 2020), HC@ NiCoLDH (Zhang et al. 2021), rGO@CoNi₂S₄@NiCo LDH (Chang et al. 2021), NiCo-LDH/NiCoP @NiMn-LDH (Liang et al. 2018).

In light of the correlation between peak current and scanning speed, we further examined the electrochemical energy storage mechanism of NiMnS @NiCoLDH@CCs and NiCoLDH@CCs by CV curves (Fig. 4c, d and Additional file 1: equation S6). The capacitive contribution of NiMnS @NiCoLDH@CCs and NiCoLDH@CCs at 50 mV s⁻¹ are 90.9% and 80.6%, respectively, corresponding to the diffusion-controlled contributions of 9.1%, and 19.4% (Fig. 4f, Additional file 1: Fig. S11b and Table S2). It confirms that the faradaic redox reactions for NiMnS @NiCoLDH@CCs have prominent contribution to offer high capacity and satisfactory rate, which is probably due to multivariate metal components and ample heterojunction interfaces.

Additional file 1: Fig. S12 clearly shows that NiMnS @NiCoLDH@CCs electrode (91.1%) has higher capacity retention than NiCoLDH@CCs electrode (89.9%) after 10,000 cycles at 10 A g⁻¹, and those coulombic efficiencies approximately reach 100%. It reveals a remarkable cycling stability of NiMnS @NiCoLDH@CCs. SEM images (Additional file 1: Fig. S13) reflect that the morphology of NiMnS @NiCoLDH@CCs remains unchanged before and after 10 000 cycles charging and discharging, vigorously certifying the outstanding structural stability. Then, we deeply analyzed EIS spectra of three CCs-based electrodes (Fig. 4g), the equivalent circuit is presented in Additional file 1: Fig. S14b. In the high frequency range, the R_{ct} for NiMnS @NiCoLDH@CCs (0.15Ω) is significantly lower than those for NiCoLDH@CCs (0.62Ω) and CCs (2.49Ω) (Additional file 1: Fig. S14a and Table S2). It implies that the NiMnS @NiCoLDH@CCs electrode has the lowest charge transfer resistance, suggesting the greater electron transfer kinetics. Besides, it distinctly displays that the NiMnS @NiCoLDH@CCs electrode shows the shortest Warburg impedance zone and the most perfect straight line in the low frequency region, implying the diffusion resistance of electrolyte ions is the minimum. These benefits result from the hollow and porous structure and numerous conductive active sites. It not only speeds up the reaction kinetics, but also promotes electrolyte transport

Overall, the advanced electrochemical activity of NiMnS @NiCoLDH@CCs microspheres is ascribed to the own outstanding structure and composition (Fig. 4h). Firstly, NiMnS @NiCoLDH@CCs has a multi-conductor structure, including inner layer conductive

CCs biochar, outer layer of NiCoLDH nanosheets and NiMnS particles. Therefore, there are multiple charge storage principles with double-layer electric capacitor, pseudocapacitor principle and electron insertion principle. Secondly, the abundant heterogeneous interface enriches the active sites, reduce the interface resistance, and improve the electron transfer rate. Then, the hollow and porous structure of LDHs offer abundant inner and outer accessible surfaces, available inner hollow space, and large specific surface area, promoting electrolyte transport and enhancing electrode reaction kinetics. Finally, multicomponent metals (Ni, Co, and Mn) and multicomponent nonmetals (S and N) effectively promote charge transfer. Consequently, NiMnS @NiCoLDH@CCs achieves remarkable specific capacitance and excellent multiplier performance due to the synergistic effect.

A rechargeable asymmetric supercapacitor (ASC) was successfully put together to further characterize the actual use of NiMnS @NiCoLDH@CCs for energy storage. Additional file 1: Fig. S15 shows a classic ASC configuration, composed of NiMnS @NiCoLDH@CCs as positive electrode and CCs as negative electrode, respectively. In combination with the potential window range that is compatible with NiMnS @NiCoLDH@CCs and CCs, Fig. 5a demonstrates that the operational voltage of the assembled NiMnS @NiCoLDH@CCs // CCs ASC device can reach 1.5 V. If the potential window is greater than 1.5 V, a clear polarization current is seen (Additional file 1: Fig. S16a and S16b). Moreover, the shape of the CV curve barely changed when the scanning rate increased from 10 to 300 mV s⁻¹ (Additional file 1: Fig. S16c), indicating better rate and reversibility properties.

As shown in the GCD curves (Fig. 5b), all discharge and charge curves are essentially symmetrical at current densities ranging from 1 to 10 A g⁻¹, implying favorable capacitance and coulombic efficiency. The corresponding specific capacitances of NiMnS @NiCoLDH@CCs // CCs ASC (Fig. 5c) are 260.9, 250.1, 243.9, 239.4, and 235.8 F g⁻¹ at current densities of 1, 2, 5, 8, 10, respectively, and surpass the reported literature (Additional file 1: Table S4). Further, even at high current density of 10 A g⁻¹, it retains high-capacity retention of 90.4%, proving the exceptional rate capability. Besides, Fig. 5d exhibits the internal resistance (R_s) and charge transfer resistance (R_{ct}) of NiMnS @NiCoLDH@CCs // CCs ASC is 0.81 Ω and 1.2 Ω, respectively, revealing the high ion diffusion and fast electron transmission. The favorable capacitance was maintained at 91.8% and the coulombic efficiency was as high as 100%, after 10 000 cycles at 5 A g⁻¹, clearly demonstrating the significant electrochemical reversibility and stability for NiMnS @NiCoLDH@CCs // CCs ASC device (Fig. 5e). The CV curves shape

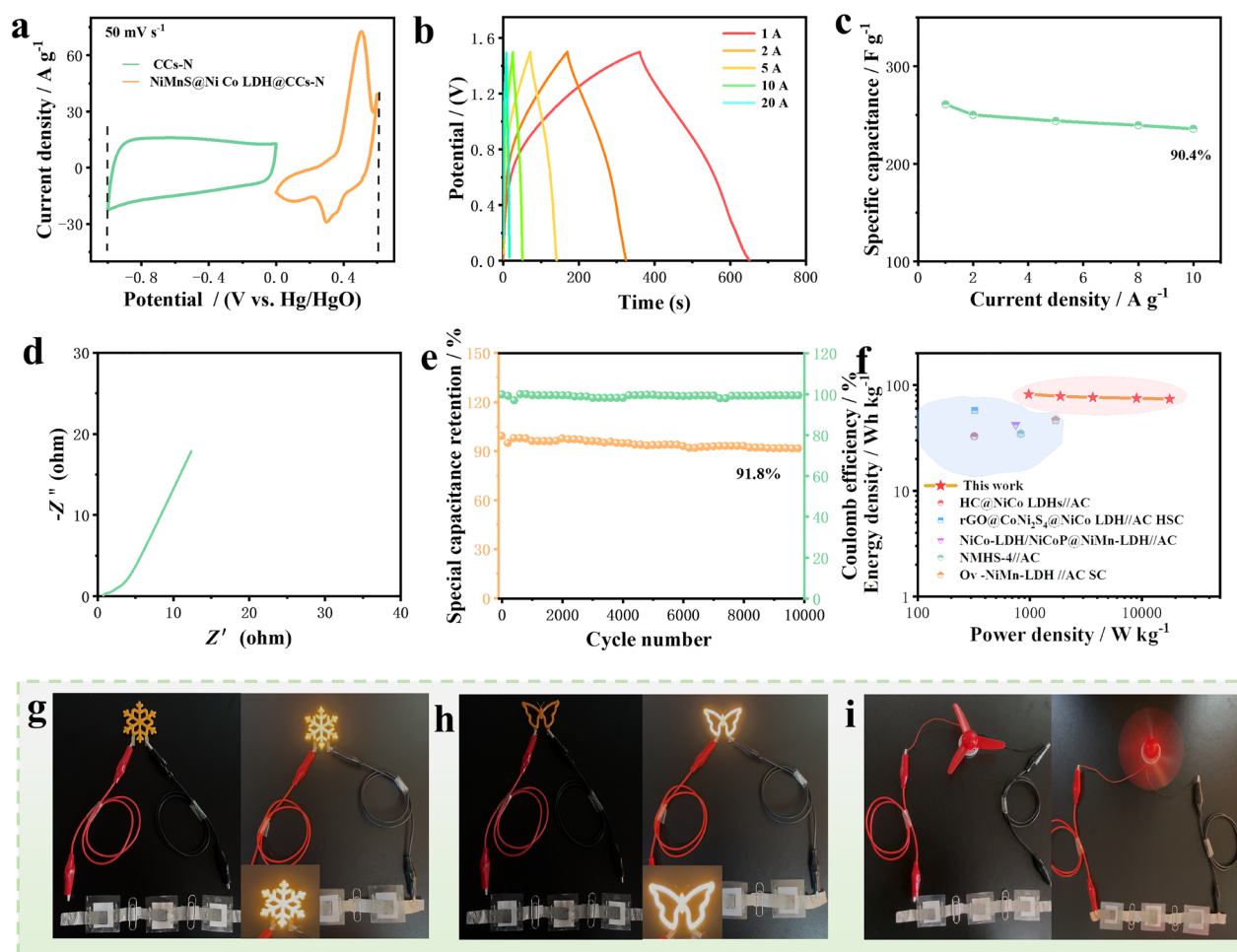


Fig. 5 The electrochemical performance of NiMnS@NiCoLDH@CCs // CCs ASC in the two-electrode (6 M KOH). **a** CV of NiMnS@NiCoLDH@CCs electrode and CCs electrode at 50 mV s^{-1} . **b** GCD with diverse current densities. **c** The specific capacitance with diverse current densities. **d** Nyquist plot of the electrochemical impedance spectra. **e** The Cycling stability and columbic efficiency. **f** Three NiMnS@NiCoLDH@CCs//CCs ASCs in series drive **g** and **h** LED lamps and **i** a small fan. **g** and **h** LED lights **i** a small fan

before and after 10 000 cycles barely changed (Additional file 1: Fig. S17a), and, the GCD curves of the last two cycles maintained a similar shape to those of the first two cycles (Additional file 1: Fig. S17b), further verifying outstanding electrochemical stability.

Impressively, the Ragone plot (Fig. 5f) displays the NiMnS@NiCoLDH@CCs // CCs ASC has favorable maximum energy density of 81.5 W h kg^{-1} at power density of 978.4 W kg^{-1} and 73.9 W h kg^{-1} at high power density of 17.7 W kg^{-1} , outperforming previously reported ASCs (Additional file 1: Table S4). Its significant performance is ascribed to its distinctive heterogeneous structure, hollow and porous structure. Furthermore, Fig. 5g–i depicts that three fully charged NiMnS@NiCoLDH@CCs // CCs ASC in series enable light-emitting diode (LED) lights and a fan to stably work, suggesting its great potential application for electronic devices. The

ASC device's remarkable cycle stability and high specific capacitance performance are ascribed to its distinctive heterogeneous structure, which is hollow and porous.

3.4 Electrocatalytic performance

The electrocatalytic activity of HER and OER for NiMnS@NiCoLDH@CCs were studied in 1 M KOH. Additional file 1: Fig. S6a displays the polarization curves of NiMnS@NiCoLDH@CCs, NiCoLDH, NiMnS, CCs after a 90% ohmic potential drop (IR) correction. Notably, the NiMnS@NiCoLDH@CCs expresses favorable HER activity with an initial overpotential closer to zero. Moreover, Fig. 6b evidences that the NiMnS@NiCoLDH@CCs possesses the smallest overpotential of 97.8 mV at 10 mV cm^{-2} , greatly lower than that of NiCoLDH (159.8 mV), NiMnS (125.6 mV) and CCs (199.2 mV), as

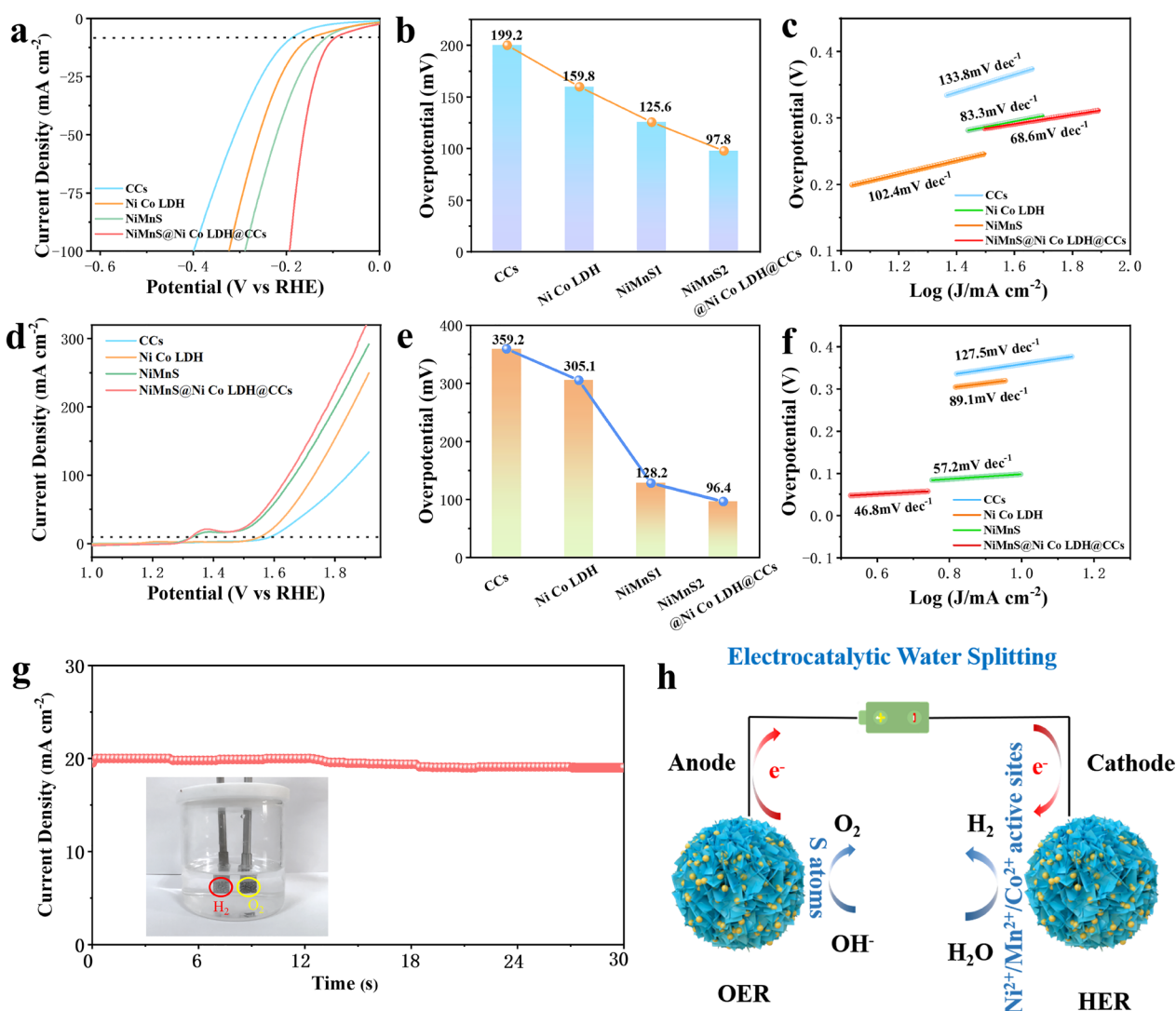


Fig. 6 HER catalytic activity of NiMnS@NiCoLDH@CCs, NiCoLDH, NiMnS, CCs in 1 M KOH. **a** LSV curves at 10 mV s⁻¹. **b** Comparison of overpotentials at 10 mA cm⁻². **c** Tafel plots. HER catalytic activity: **d** LSV curves at 10 mV s⁻¹. **e** Comparison of overpotentials at 10 mA cm⁻². **f** Tafel plots. **g** The i-t curves of overall water electrolysis for NiMnS@NiCoLDH@CCs||NiMnS@NiCoLDH@CCs at the potential of 20 mV for 30 h. (Inset: The image of H₂ and O₂ bubbles on electrodes in testing). **h** Schematic illustration of OER and HER mechanism of NiMnS@NiCoLDH@CCs

well as most reported same type electrocatalysts (Additional file 1: Table S5), such as NiCo/NiCo₂S₄@NiCo/NF ($\eta_{10\text{mA cm}^{-2}}=132\text{ mV}$) (Ning et al. 2018), NiMn HNSs ($\eta_{10\text{mA cm}^{-2}}=302\text{ mV}$) (Sun et al. 2017), NF@Ni₃S₂-NiOOH ($\eta_{10\text{mA cm}^{-2}}=123\text{ mV}$) (Wang et al. 2018), CoNiSx/NF-25 ($\eta_{10\text{mA cm}^{-2}}=123\text{ mV}$) (Lu et al. 2019), Ni_xSy@MnOxHy/NF ($\eta_{10\text{mA cm}^{-2}}=179\text{ mV}$) (Wang et al. 2022). Figure 6c shows that NiMnS@NiCoLDH@CCs achieves fast HER kinetics, as evidenced by a low Tafel slope of 68.6 mV dec⁻¹, which is lower than that of NiCoLDH (83.3 mV dec⁻¹), NiMnS (102.4 mV dec⁻¹) and CCs (133.8 mV dec⁻¹) and recent reported materials (Additional file 1: Table S5). It further manifests that the

establishment of multi-interface heterojunction structure of NiMnS@NiCoLDH@CCs enables the catalyst to highly accelerate reaction kinetics. It further manifests that the establishment of multi-interface heterojunction structure of NiMnS@NiCoLDH@CCs enables the catalyst to highly accelerate reaction kinetics. According to the Tafel slope value of NiMnS@NiCoLDH@CCs ranging from 39 to 118 mV dec⁻¹, the speed limiting step of HER conforms to the Volmer-Heyrovsky process (Li et al. 2019b). To better comprehend the relationship between HER performance and intrinsic activity of the catalyst, the electrochemical active surface area (ECSA) of each electrode was analyzed and compared. Generally,

the value of electrochemical double-layer capacitance (Cdl) is proportional to the value of ECSA, and it can be obtained through the CV curves with different sweep speeds in the non-Faraday potential range. As shown in Additional file 1: Fig. S16 a and 16b, the Cdl value of NiMnS @NiCoLDH@CCs (7.38 m F cm^{-2}) is significantly higher than that of NiMnS (3.79 m F cm^{-2}), NiCoLDH (2.09 m F cm^{-2}) and CCs (1.75 m F cm^{-2}). The results indicate that NiMnS @NiCoLDH@CCs has more electrochemical active area, which is beneficial to expose more active sites.

Similarly, the OER electrocatalytic performance of NiMnS @NiCoLDH@CCs was further studied in 1 M KOH solution. As shown in Fig. 6d, contrasted with those samples, the polarization curve of NiMnS @NiCoLDH@CCs with 90% iR correction depicts faster anodic current rise beyond onset potential. The peak at 1.36 V is attributed to the oxidation of Ni^{2+} to Ni^{3+} (Ning et al. 2018). Figure 6e reveals that the overpotential of NiMnS @NiCoLDH@CCs (96.4 mV) at 10 mA cm^{-2} is much lower than that of NiMnS (128.2 mV), NiCoLDH (305.1 mV), CCs (359.2 mV) and most reported electrocatalysts (Additional file 1: Table S6), such as NiS@CoNi₂S₄/NC ($\eta_{10 \text{ mA cm}^{-2}} = 126 \text{ mV}$) (Dang et al. 2023), Ni-Co-S HPNA ($\eta_{10 \text{ mA cm}^{-2}} = 270 \text{ mV}$) (Chen et al. 2020), Mn-Co₃O₄/S ($\eta_{10 \text{ mA cm}^{-2}} = 330 \text{ mV}$) (Qi et al. 2019), MCCF/NiMn-MOFs ($\eta_{10 \text{ mA cm}^{-2}} = 280 \text{ mV}$) (Cheng et al. 2020). Additionally, the Tafel plot (Fig. 6f) of NiMnS.

@NiCoLDH@CCs is 68.6 mV dec^{-1} , preferable to that of NiCoLDH (83.3 mV dec^{-1}), NiMnS ($102.4 \text{ mV dec}^{-1}$) and CCs ($133.8 \text{ mV dec}^{-1}$), which is comparable to many other recent reported materials (Additional file 1: Table S6). These results suggest that NiMnS @NiCoLDH@CCs is a superior active bifunctional electrocatalyst for practical applications. Additional file 1: Fig. S16b and c demonstrate the Cdl value of NiMnS @NiCoLDH@CCs ($10.68 \text{ m F cm}^{-2}$) significantly higher than that of NiMnS (5.98 m F cm^{-2}), NiCoLDH (3.37 m F cm^{-2}) and CCs (1.06 m F cm^{-2}). The results indicate that NiMnS @NiCoLDH@CCs has more active sites, which is beneficial for OER performance.

Based on the outstanding performance of both HER and OER in alkaline electrolyte, NiMnS@NiCoLDH@CCs was employed as both anode and cathode to assemble alkaline electrolytic cell for overall water electrolysis (Fig. 6g Inset). As shown in the Additional file 1: Fig. S17, NiMnS @NiCoLDH@CCs||NiMnS @NiCoLDH@CCs exhibited superior performance with a low cell voltage of 1.49 V at 10 mA cm^{-2} , preceding previously reported electrocatalysts (Additional file 1: Table S7), such as NiS/Ni₂P/CC (Xiao et al. 2018), NiCo LDH/NF (Shang et al. 2022), CoNi₂S₄@NiMn LDH/SCC (Wang et al. 2020), NiCo/NiCo₂S₄@NiCo/NF (Ning et al. 2018), CuO_xNWs@

NiMnO_xNSs (Tang et al. 2017). Besides, Fig. 6g inset shows that a mass of H₂ and O₂ bubbles are observed on both anode and cathode electrodes during water electrolysis process. Importantly, the current density barely declined after 30 h continuous test, suggesting excellent durability and stability. The Faradaic efficiency (F%) was also investigated by comparing experimentally produced H₂ and O₂ with the theoretically calculated ones at 10 mA for 1 h (Additional file 1: Fig. S20a). The average Faraday efficiency of HER and OER was 98.2% and 98.0% (Additional file 1: Fig. S20b), respectively, which surpasses that of previously reported electrocatalysts (Additional file 1: Table S8). It further indicates that the electrocatalyst with high Faraday efficiency has strong electron transfer ability and high efficiency of the electrode reaction.

Totally, the advanced electrocatalytic activity of NiMnS @NiCoLDH@CCs results from the own improved structure (Fig. 6h). Firstly, the plenty heterojunction interface between NiMnS and NiCoLDH facilitates electrolyte ion adsorption, and expedites the breakdown of O–H bonds for correlative substance, further accelerating reaction kinetics (Sirisomboonchai et al. 2020). Secondly, the unique porous and hollow structure provides numerous active sites to accelerate charge transfer, but also offers larger inner cavities and nanopore channels for the NiCoLDH to promote electrolyte transport. Moreover, bimetallic sulfides have good electrochemical activity and abundant active sites. Finally, the conductive biochar matrix provides structural stability. Hence, the above synergy jointly promotes the electrocatalyst performance of NiMnS @ NiCoLDH @ CCs.

According to the above findings, NiMnS@NiCoLDH@CCs is a multifunctional electrode material that achieves both the electrocatalyst of HER, OER and supercapacitors. Based on the demands of practical applications, we built a coupled energy storage device and hydrogen production system (CEHS), which availably guarantees the efficient and stable operation of electrolytic hydrogen production system (Additional file 1: Fig. S18a). Particularly, when the main circuit stops supplying energy due to external interference, the spare supercapacitor will immediately provide stable energy output to ensure the normal and continuous operation of the hydrogen production system. Additional file 1: Fig. S18b and c displays the CEHS based on NiMnS@NiCoLDH@CCs material, which consists of a three-series SCs and overall water electrolysis device. Notably, the device successfully drove water electrolysis and demonstrated excellent performance (Fig. 7a and Additional file 2: Video S1). Figure 7a shows an enlarged view of the overall water electrolysis, accompanied by stable steady H₂ and O₂ generation with numerous bubbles. These results demonstrate the great potential of multifunctional biomass microspheres with

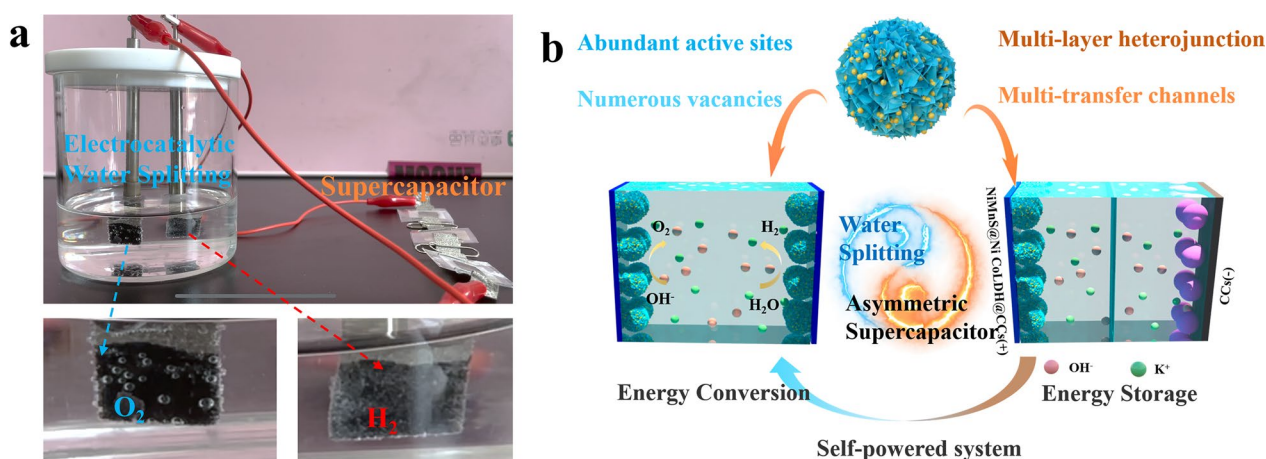


Fig. 7 **a** A picture of the CEHS coupled system and enlarged pictures for O_2 and H_2 evolutions. **b** The mechanisms illustration of enhanced electrochemical performance

heterogeneous structures in integrated energy storage and conversion systems. The NiMnS @NiCoLDH@CCs electrode has superior electrochemical performance on account of its preminent structure and materials. The reasons are as follows (Fig. 7b). First, three-dimensional layered conductors composed of conductive biomass carbon microspheres and abundant heterojunctions are established with abundant interface, which effectively accelerates electron transfer and highly reduces electrochemical polarization. Second, numerous porous and hollow structures expose plenty active sites, contributing to superior molecular permeability and efficient gas release channels, and reduce concentration polarization. Third, bimetallic sulfides and polymetallic doping markedly advance the catalytic activity of active sites and further improve electrochemical activity.

4 Conclusions

In summary, a conductive and multifunctional chitosan biochar microsphere by a facile emulsion crosslinking, solution growth and hydrothermal sulphuration method, was successfully constructed. The attained multifunctional electrode material simultaneously achieved both the electrocatalyst of HER, OER and supercapacitors due to preminent structure and materials. Moreover, three-dimensional layered conductors composed of conductive biochar microspheres and abundant heterojunctions were constructed with abundant interface, hollow and porous structure, which effectively accelerate electron transfer and highly reduces electrochemical polarization. Consequently, the NiMnS @NiCoLDH@CCs as electrode achieved a high specific capacitance of 3072.6 F g^{-1} at 1 A g^{-1} . Importantly, NiMnS @NiCoLDH@CCs //

CCs ASC realized a high specific capacitance of 260.9 F g^{-1} at 1 A g^{-1} and remarkable energy density of 81.5 W h kg^{-1} at power density of 978.4 W kg^{-1} . And it had superior cycling performance maintaining 91.8% after 10,000 cycles at 10 A g^{-1} . Besides, the NiMnS @NiCoLDH@CCs as an electrode for electrolysis, only required a low cell voltage of 1.49 V to achieve a current density of 10 mA cm^{-2} and achieve superior stability and durability with 30 h continuous test at 50 mA cm^{-2} . We used this electrode material to innovatively design a coupled energy storage device and hydrogen production system. As a backup power, coupled SCs with high energy density can effectually assure the extremely efficient and stable operation of the overall water electrolysis without the manipulation of main power due to changes in the external environment. Our study provides a promising strategy for designing integrated electrode materials based on multifunctional biochar microspheres with heterogeneous structures in integrated energy storage and conversion systems.

Supplementary Information

The online version contains supplementary material available at <https://doi.org/10.1007/s42773-023-00266-2>.

Additional file 1: Figure S1. (a) SEM of CCs. (b) TEM of CCs. (c) EDS of CCs. **Figure S2.** FTIR spectrum of (a) Cs-based materials (b) NiMnS @ Ni Co LDH@CCs materials, respectively. **Figure S3.** EDS of Ni Co LDH@CCs. **Figure S4.** HRTEM images of NiMnS @Ni Co LDH@CCs. **Figure S5.** (a-d) SEM images of Ni Co LDH@CCs with different Ni^{2+}/Co^{2+} concentration of 0, 0.1 mM, 0.3 mM, 0.5 mM at different magnification, respectively. **Figure S6.** (a-c) SEM images of NiMnS @Ni Co LDH@CCs with different S concentration at different magnification. **Figure S7.** XRD patterns of (a) Cs sphere (b) NiMnS @Ni Co LDH@CCs, respectively. **Figure S8.** (a) N_2 adsorption/desorption (d) Pore distribution of CCs, Ni Co LDH@CCs, NiMnS @ Ni Co LDH@CCs, respectively. **Figure S9.** Ni^{3+}/Ni^{2+} ratios for Ni Co LDH@

CCs and NiMnS@NiCoLDH@CCs in Ni 2p spectrum. **Figure S10.** The CV of CCs-700, CCs-800, CCs-900, respectively. **Figure S11.** GCD curves of the NiCoLDH@CCs electrodes at different current densities. (b) Comparison of capacitive-controlled contribution for energy storage for NiCoLDH@CCs at various scan rates. (c, d) The capacitive and diffusion-controlled contribution of NiCoLDH@CCs, NiMnS@NiCoLDH@CCs samples at 50 mV s⁻¹, respectively. **Figure S12.** (a, b) Cycling stability and coulombic efficiency after 10000 cycles of the NiMnS@NiCoLDH@CCs, NiCoLDH@CCs electrodes, respectively. **Figure S13.** SEM image of the NiMnS@NiCoLDH@CCs electrode (a) before and (b) after 10000 cycles charging and discharging. **Figure S14.** (a) Histogram of Rct for NiMnS@NiCoLDH@CCs samples electrode. (b) The corresponding equivalent circuit for fitting the Impedance Nyquist plots. **Figure S15.** Structure image of NiMnS@NiCoLDH@CCs // CCs ASC. **Figure S16.** (a) The GCD curves and (b) CV curves of NiMnS@NiCoLDH@CCs // CCs ASCs at different potential ranges. (c) CV curves of NiMnS@NiCoLDH@CCs // CCs ASCs electrode at various scan rate. **Figure S17.** (d) CV curves and (e) GCD curves of NiMnS@NiCoLDH@CCs // CCs ASCs before and after 10000 cycles. **Figure S18.** (a) CV recorded for NiMnS@NiCoLDH@CCs electrode in the approximate region of 0.1–0.18 V vs. RHE at various scan rates, respectively. (b) Plot showing the extraction of the double-layer capacitance (C_{dl}) of NiMnS@NiCoLDH@CCs for HER. (c) CV recorded for NiMnS@NiCoLDH@CCs electrode in the approximate region of 0.28–0.32 V vs. RHE at various scan rates, respectively. (d) Plot showing the extraction of the double-layer capacitance (C_{dl}) of NiMnS@NiCoLDH@CCs for OER. **Figure S19.** Polarization curves of the NiMnS@NiCoLDH@CCs||NiMnS@NiCoLDH@CCs for overall water splitting in 1 M KOH. **Figure S20.** (a) Oxygen and hydrogen production tests in 1 M KOH. (b) Faraday efficiency. **Figure S21.** (a) The circuit diagram of coupled energy storage device and hydrogen production system. (a) The schematic of coupled energy storage device and hydrogen production system. The OWE device can be driven by the SCs full cell. (c) The photos of coupled energy storage device and hydrogen production system. **Table S1.** The contents of NiCoLDH@CCs based materials from XPS. **Table S2.** The Electrochemical parameters of the NiCoLDH@CCs, NiMnS@NiCoLDH@CCs. **Table S3.** The comparison of specific capacity between NiMnS@NiCoLDH@CCs electrode and other recently reported works. **Table S4.** The comparison of energy density and power density between NiMnS@NiCoLDH@CCs // CCs ASC supercapacitor and other supercapacitors. **Table S5.** Comparison of HER activity of various nonprecious catalysts in 1 M KOH. **Table S6.** Comparison of OER activity of various nonprecious catalysts in 1 M KOH. **Table S7.** Comparison of overall water splitting activity of various nonprecious bifunctional catalysts in 1 M KOH solution. **Table S8.** Comparison of overall water Faraday efficiency of various catalysts in 1 M KOH solution.

Additional file 2. The coupled energy storage and hydrogen production device successfully drives water electrolysis.

Acknowledgements

The authors greatly acknowledge the support of the Pan Chen and Beijing Natural Science Foundation.

Author contributions

CY: Conceptualization, Investigation, Data curation, Writing—Original draft preparation. YY: Formal analysis, Software, Supervision. JW: Visualization, Investigation. JH: Supervision, Writing—Reviewing. ZS: Supervision, Methodology, Writing—Reviewing and Editing.

Funding

This study was funded Beijing Natural Science Foundation from Pan Chen.

Availability of data and materials

The corresponding author can provide the datasets upon an adequate request.

Declarations

Competing interests

The all authors have no financial or proprietary interests with other people or organizations.

Author details

¹Beijing Engineering Research Center of Cellulose and Its Derivatives, School of Materials Science and Engineering, Beijing Institute of Technology, Beijing 100081, People's Republic of China. ²College of Environmental Science and Engineering, Yangzhou University, Yangzhou, Jiangsu 225009, People's Republic of China.

Received: 9 May 2023 Revised: 17 September 2023 Accepted: 22 September 2023

Published online: 15 December 2023

References

- Abd El-Monaem EM, Elshishini HM, Bakr SS, El-Aqapa HG, Hosny M, Andaluri G, El-Subruiti GM, Omer AM, Eltaweil AS (2023) A comprehensive review on LDH-based catalysts to activate persulfates for the degradation of organic pollutants. *NPJ Clean Water*. <https://doi.org/10.1038/s41545-023-00245-x>
- Aswathy NR, Palai AK, Ramadoss A, Mohanty S, Nayak SK (2020) Fabrication of cellulose acetate-chitosan based flexible 3D scaffold-like porous membrane for supercapacitor applications with PVA gel electrolyte. *Cellulose* 27:3871–3887. <https://doi.org/10.1007/s10570-020-03030-y>
- Avril C, Malavergne V, Caracas R, Zanda B, Reynard B, Charon E, Bobocioiu E, Brunet F, Borensztajn S, Pont S et al (2013) Raman spectroscopic properties and Raman identification of CaS-MgS-MnS-FeS-Cr₂FeS₄sulfides in meteorites and reduced sulfur-rich systems. *Meteorit Planet Sci* 48:1415–1426. <https://doi.org/10.1111/maps.12145>
- Ayodele TR, Munda JL (2019) Potential and economic viability of green hydrogen production by water electrolysis using wind energy resources in South Africa. *Int J Hydrogen Energy* 44:17669–17687. <https://doi.org/10.1016/j.ijhydene.2019.05.077>
- Borenstein A, Hanna O, Attias R, Luski S, Brousse T, Aurbach D (2017) Carbon-based composite materials for supercapacitor electrodes: a review. *J Mater Chem A* 5:12653–12672. <https://doi.org/10.1039/c7ta00863e>
- Chang J, Zang S, Liang W, Wu D, Lian Z, Xu F, Jiang K, Gao Z (2021) Enhanced faradic activity by construction of p-n junction within reduced graphene oxide@cobalt nickel sulfide@nickel cobalt layered double hydroxide composite electrode for charge storage in hybrid supercapacitor. *J Colloid Interface Sci* 590:114–124. <https://doi.org/10.1016/j.jcis.2021.01.035>
- Chen W, Zhang Y, Chen G, Huang R, Wu Y, Zhou Y, Hu Y, Ostrikov KK (2020) Hierarchical porous bimetal-sulfide bi-functional nanocatalysts for hydrogen production by overall water electrolysis. *J Colloid Interface Sci* 560:426–435. <https://doi.org/10.1016/j.jcis.2019.10.099>
- Cheng W, Lu XF, Luan D, Lou XWD (2020) NiMn-based bimetal-organic framework nanosheets supported on multi-channel carbon fibers for efficient oxygen electrocatalysis. *Angew Chem Int Ed Engl* 59:18234–18239. <https://doi.org/10.1002/anie.202008129>
- Choudhary N, Li C, Moore J, Nagaiah N, Zhai L, Jung Y, Thomas J (2017) Asymmetric supercapacitor electrodes and devices. *Adv Mater*. <https://doi.org/10.1002/adma.201605336>
- Dang J, Yun S, Zhang Y, Yang G, Yang J, Qiao D, Yang T (2023) Designing nitrogen-enriched heterogeneous NiS@CoNi (2)S (4) embedded in nitrogen-doped carbon with hierarchical 2D/3D nanocage structure for efficient alkaline hydrogen evolution and triiodide reduction. *J Colloid Interface Sci* 630:91–105. <https://doi.org/10.1016/j.jcis.2022.09.136>
- Du X, Huang J, Zhang J, Yan Y, Wu C, Hu Y, Yan C, Lei T, Chen W, Fan C et al (2019) Modulating electronic structures of inorganic nanomaterials for efficient electrocatalytic water splitting. *Angew Chem Int Ed Engl* 58:4484–4502. <https://doi.org/10.1002/anie.201810104>
- Eltaweil AS, Bakr SS, Abd El-Monaem EM, El-Subruiti GM (2023) Magnetic hierarchical flower-like Fe (3)O (4)@ZIF-67/CuNiMn-LDH catalyst with enhanced redox cycle for Fenton-like degradation of Congo red: optimization and mechanism. *Environ Sci Pollut Res Int* 30:75332–75348. <https://doi.org/10.1007/s11356-023-27430-2>

- Fan H, Huang J, Chen G, Chen W, Zhang R, Chu S, Wang X, Li C, Ostrikov KK (2018) Hollow Ni–V–Mo chalcogenide nanopetals as bifunctional electrocatalyst for overall water splitting. *ACS Sustain Chem Eng* 7:1622–1632. <https://doi.org/10.1021/acssuschemeng.8b05378>
- Gong F, Ye S, Liu M, Zhang J, Gong L, Zeng G, Meng E, Su P, Xie K, Zhang Y et al (2020) Boosting electrochemical oxygen evolution over yolk-shell structured O-MoS₂ nanostructures with sulfur vacancy and decorated Pt nanoparticles. *Nano Energy*. <https://doi.org/10.1016/j.nanoen.2020.105284>
- Han W-B, Kim I-S, Kim M, Cho WC, Kim S-K, Joo JH, Lee Y-W, Cho Y, Cho H-S, Kim C-H (2021) Directly sputtered nickel electrodes for alkaline water electrolysis. *Electrochim Acta*. <https://doi.org/10.1016/j.electacta.2021.138458>
- He W, Ifraemov R, Raslin A, Hod I (2018) Room-temperature electrochemical conversion of metal-organic frameworks into porous amorphous metal sulfides with tailored composition and hydrogen evolution activity. *Adv Funct Mater*. <https://doi.org/10.1002/adfm.201707244>
- Hu D, Zhang Y, Lin J, Hou Y, Li D, Wu T (2017) Dual emissions from MnS clusters confined in the sodalite nanocage of a chalcogenide-based semiconductor zeolite. *Dalton Trans* 46:3929–3933. <https://doi.org/10.1039/c7dt00386b>
- Huang ZF, Song J, Li K, Tahir M, Wang YT, Pan L, Wang L, Zhang X, Zou JJ (2016) Hollow cobalt-based bimetallic sulfide polyhedra for efficient all-pH-value electrochemical and photocatalytic hydrogen evolution. *J Am Chem Soc* 138:1359–1365. <https://doi.org/10.1021/jacs.5b11986>
- Huang S, Wang J, Pan Z, Zhu J, Shen PK (2017) Ultrahigh capacity and superior stability of three-dimensional porous graphene networks containing in situ grown carbon nanotube clusters as an anode material for lithium-ion batteries. *J Mater Chem A* 5:7595–7602. <https://doi.org/10.1039/c6ta11191b>
- Kang C, Ma L, Chen Y, Fu L, Hu Q, Zhou C, Liu Q (2022) Metal-organic framework derived hollow rod-like NiCoMn ternary metal sulfide for high-performance asymmetric supercapacitors. *Chem Eng J*. <https://doi.org/10.1016/j.cej.2021.131003>
- Kuang Y, Yamada T, Domen K (2017) Surface and interface engineering for photoelectrochemical water oxidation. *Joule* 1:290–305. <https://doi.org/10.1016/j.joule.2017.08.004>
- Li JG, Sun H, Lv L, Li Z, Ao X, Xu C, Li Y, Wang C (2019a) Metal-organic framework-derived hierarchical (Co, Ni)Se (2)@NiFe LDH hollow nanocages for enhanced oxygen evolution. *ACS Appl Mater Interfaces* 11:8106–8114. <https://doi.org/10.1021/acami.8b22133>
- Li W, Liu G, Li J, Wang Y, Ricardez-Sandoval L, Zhang Y, Zhang Z (2019b) Hydrogen evolution reaction mechanism on 2H-MoS₂ electrocatalyst. *Appl Surf Sci*. <https://doi.org/10.1016/j.apsusc.2019.143869>
- Li L, Zhang D, Deng J, Gou Y, Fang J, Cui H, Zhao Y, Cao M (2021a) Carbon-based materials for fast charging lithium-ion batteries. *Carbon* 183:721–734. <https://doi.org/10.1016/j.carbon.2021.07.053>
- Li Z, Hu M, Wang P, Liu J, Yao J, Li C (2021b) Heterojunction catalyst in electrocatalytic water splitting. *Coord Chem Rev*. <https://doi.org/10.1016/j.ccr.2021.213953>
- Liang H, Lin J, Jia H, Chen S, Qi J, Cao J, Lin T, Fei W, Feng J (2018) Hierarchical NiCo-LDH/NiCoP@NiMn-LDH hybrid electrodes on carbon cloth for excellent supercapacitors. *J Mater Chem A* 6:15040–15046. <https://doi.org/10.1039/c8ta05065a>
- Libich J, Máca J, Vondrák J, Čech O, Sedlářiková M (2018) Supercapacitors: properties and applications. *J Energy Storage* 17:224–227. <https://doi.org/10.1016/j.est.2018.03.012>
- Lin Z, Liu S, Liu Y, Liu Z, Zhang S, Zhang X, Tian Y, Tang Z (2021) Rational design of Ru aerogel and RuCo aerogels with abundant oxygen vacancies for hydrogen evolution reaction, oxygen evolution reaction, and overall water splitting. *J Power Sour*. <https://doi.org/10.1016/j.jpowsour.2021.230600>
- Lu L, Xu X, An K, Wang Y, Shi F-N (2018) Coordination polymer derived NiS@g-C₃N₄ composite photocatalyst for sulfur vacancy and photothermal effect synergistic enhanced H₂ production. *ACS Sustain Chem Eng* 6:11869–11876. <https://doi.org/10.1021/acssuschemeng.8b02153>
- Lu W, Li X, Wei F, Cheng K, Li W, Zhou Y, Zheng W, Pan L, Zhang G (2019) In-situ transformed Ni, S-codoped CoO from amorphous Co–Ni sulfide as an efficient electrocatalyst for hydrogen evolution in alkaline media. *ACS Sustain Chem Eng*. <https://doi.org/10.1021/acssuschemeng.9b02216>
- Luo F, Hu H, Zhao X, Yang Z, Zhang Q, Xu J, Kaneko T, Yoshida Y, Zhu C, Cai W (2020) Robust and stable acidic overall water splitting on Ir single atoms. *Nano Lett* 20:2120–2128. <https://doi.org/10.1021/acs.nanolett.0c00127>
- Ning Y, Ma D, Shen Y, Wang F, Zhang X (2018) Constructing hierarchical mushroom-like bifunctional NiCo/NiCo₂S₄@NiCo/Ni foam electrocatalysts for efficient overall water splitting in alkaline media. *Electrochim Acta* 265:19–31. <https://doi.org/10.1016/j.electacta.2018.01.150>
- Omer AM, Elgarhy GS, El-Subruiti GM, Abd El-Monaem EM, Eltaweil AS (2023) Construction of efficient Ni-FeLDH@MWCNT@Cellulose acetate floatable microbeads for Cr (VI) removal: performance and mechanism. *Carbohydr Polym* 311:120771. <https://doi.org/10.1016/j.carbpol.2023.120771>
- Ong W-J, Shak KPY (2020) 2D/2D Heterostructured photocatalysts: an emerging platform for artificial photosynthesis. *Solar RRL*. <https://doi.org/10.1002/solr.202000132>
- Qi J, Wang H, Lin J, Li C, Si X, Cao J, Zhong Z, Feng J (2019) Mn and S dual-doping of MOF-derived Co (3)O (4) electrode array increases the efficiency of electrocatalytic generation of oxygen. *J Colloid Interface Sci* 557:28–33. <https://doi.org/10.1016/j.jcis.2019.09.009>
- Rathore D, Ghosh S, Chowdhury J, Pande S (2022) Co-doped Ni₉S₈ nanostructures for electrocatalytic water splitting over a wide pH range. *ACS Appl Nano Mater* 5:11823–11838. <https://doi.org/10.1021/acsnm.2c02842>
- Roy BK, Tahmid I, Rashid TU (2021) Chitosan-based materials for supercapacitor applications: a review. *J Mater Chem A* 9:17592–17642. <https://doi.org/10.1039/d1ta02997e>
- Shang J, Xu C, Wang Q, Wang S, Chen J, Wang X (2022) Oxygen vacancies boosted by laser irradiation enable NiCo layered double hydroxide with a high oxygen reduction/evolution catalytic activity in Zn–air batteries and water splitting. *ACS Appl Energy Mater* 5:12427–12436. <https://doi.org/10.1021/acsaem.2c02062>
- Shi X, Ling X, Li L, Zhong C, Deng Y, Han X, Hu W (2019) Nanosheets assembled into nickel sulfide nanospheres with enriched Ni³⁺ active sites for efficient water-splitting and zinc–air batteries. *J Mater Chem A* 7:23787–23793. <https://doi.org/10.1039/c9ta03819a>
- Shi Y, Zhu B, Guo X, Li W, Ma W, Wu X, Pang H (2022) MOF-derived metal sulfides for electrochemical energy applications. *Energy Storage Mater* 51:840–872. <https://doi.org/10.1016/j.ensm.2022.07.027>
- Si F, Tang C, Gao Q, Peng F, Zhang S, Fang Y, Yang S (2020) Bifunctional CdS@Co₉S₈/Ni₃S₂ catalyst for efficient electrocatalytic and photo-assisted electrocatalytic overall water splitting. *J Mater Chem A* 8:3083–3096. <https://doi.org/10.1039/c9ta11921c>
- Sirisomboonchai S, Li X, Kitiphatpipoon N, Channoo R, Li S, Ma Y, Kongparakul S, Samart C, Abudula A, Guan G (2020) Fabrication of CuOx nanowires@NiMnOx nanosheets core@shell-type electrocatalysts: crucial roles of defect modification and valence states for overall water electrolysis. *J Mater Chem A* 8:16463–16476. <https://doi.org/10.1039/d0ta04172f>
- Song Y, Cheng X, Chen H, Huang J, Chen X, Han M, Su Z, Meng B, Song Z, Zhang H (2016) Integrated self-charging power unit with flexible supercapacitor and triboelectric nanogenerator. *J Mater Chem A* 4:14298–14306. <https://doi.org/10.1039/c6ta05816g>
- Sun W, Lipka SM, Swartz C, Williams D, Yang F (2016) Hemp-derived activated carbons for supercapacitors. *Carbon* 103:181–192. <https://doi.org/10.1016/j.carbon.2016.02.090>
- Sun X, Shao Q, Pi Y, Guo J, Huang X (2017) A general approach to synthesise ultrathin NiM (M = Fe, Co, Mn) hydroxide nanosheets as high-performance low-cost electrocatalysts for overall water splitting. *J Mater Chem A* 5:7769–7775. <https://doi.org/10.1039/c7ta02091k>
- Sun Z, Wang G, Koh SW, Ge J, Zhao H, Hong W, Fei J, Zhao Y, Gao P, Miao H et al (2020) Solar-driven alkaline water electrolysis with multifunctional catalysts. *Adv Funct Mater*. <https://doi.org/10.1002/adfm.202002138>
- Tan YB, Lee J-M (2013) Graphene for supercapacitor applications. *J Mater Chem A*. <https://doi.org/10.1039/c3ta12193c>
- Tang T, Jiang WJ, Niu S, Liu N, Luo H, Chen YY, Jin SF, Gao F, Wan LJ, Hu JS (2017) Electronic and morphological dual modulation of cobalt carbonate hydroxides by Mn doping toward highly efficient and stable bifunctional electrocatalysts for overall water splitting. *J Am Chem Soc* 139:8320–8328. <https://doi.org/10.1021/jacs.7b03507>
- Tang YJ, Zhang AM, Zhu HJ, Dong LZ, Wang XL, Li SL, Han M, Xu XX, Lan YQ (2018) Polyoxometalate precursors for precisely controlled synthesis of bimetallic sulfide heterostructure through nucleation-doping competition. *Nanoscale* 10:8404–8412. <https://doi.org/10.1039/c8nr00925b>

- Tang Y, Shen H, Cheng J, Liang Z, Qu C, Tabassum H, Zou R (2020) Fabrication of oxygen-vacancy abundant NiMn-layered double hydroxides for ultrahigh capacity supercapacitors. *Adv Funct Mater*. <https://doi.org/10.1002/adfm.201908223>
- Toma FM, Sartorel A, Iurlo M, Carraro M, Rapino S, Hooper-Burkhardt L, Da Ros T, Marcaccio M, Scorrano G, Paolucci F et al (2011) Tailored functionalization of carbon nanotubes for electrocatalytic water splitting and sustainable energy applications. *ChemSuschem* 4:1447–1451. <https://doi.org/10.1002/cssc.201100089>
- Wang X, Liu R, Zhang Y, Zeng L, Liu A (2018) Hierarchical Ni₃S₂-NiOOH heteronano-composite grown on nickel foam as a noble-metal-free electrocatalyst for hydrogen evolution reaction in alkaline electrolyte. *Appl Surf Sci* 456:164–173. <https://doi.org/10.1016/j.apsusc.2018.06.107>
- Wang P, Qi J, Li C, Li W, Wang T, Liang C (2020) Hierarchical CoNi₂S₄@NiMn-layered double hydroxide heterostructure nanoarrays on superhydrophilic carbon cloth for enhanced overall water splitting. *Electrochim Acta*. <https://doi.org/10.1016/j.electacta.2020.136247>
- Wang A, Sun K, Xu R, Sun Y, Jiang J (2021a) Cleanly synthesizing rotten potato-based activated carbon for supercapacitor by self-catalytic activation. *J Clean Prod*. <https://doi.org/10.1016/j.jclepro.2020.125385>
- Wang M, Zhang L, He Y, Zhu H (2021b) Recent advances in transition-metal-sulfide-based bifunctional electrocatalysts for overall water splitting. *J Mater Chem A* 9:5320–5363. <https://doi.org/10.1039/d0ta12152e>
- Wang W, Yan H, Anand U, Mirsaidov U (2021c) Visualizing the conversion of metal-organic framework nanoparticles into hollow layered double hydroxide nanocages. *J Am Chem Soc* 143:1854–1862. <https://doi.org/10.1021/jacs.0c10285>
- Wang P, Luo Y, Zhang G, Chen Z, Ranganathan H, Sun S, Shi Z (2022) Interface engineering of Ni(x)S(y)@MnO(x)H(y) nanorods to efficiently enhance overall-water-splitting activity and stability. *Nanomicro Lett* 14:120. <https://doi.org/10.1007/s40820-022-00860-2>
- Wu W, Wu X-Y, Wang S-S, Lu C-Z (2020) Phosphomolybdenic acid-bipolar membrane: an efficient and reversible coupling for alkaline water electrolysis. *ACS Sustain Chem Eng* 8:18528–18534. <https://doi.org/10.1021/acssuschemeng.0c06444>
- Xiao X, Huang D, Fu Y, Wen M, Jiang X, Lv X, Li M, Gao L, Liu S, Wang M et al (2018) Engineering NiS/Ni(2)P heterostructures for efficient electrocatalytic water splitting. *ACS Appl Mater Interfaces* 10:4689–4696. <https://doi.org/10.1021/acsami.7b16430>
- Xin Y, Kan X, Gan LY, Zhang Z (2017) Heterogeneous bimetallic phosphide/sulfide nanocomposite for efficient solar-energy-driven overall water splitting. *ACS Nano* 11:10303–10312. <https://doi.org/10.1021/acsnano.7b05020>
- Yilmaz G, Yam KM, Zhang C, Fan HJ, Ho GW (2017) In situ transformation of MOFs into layered double hydroxide embedded metal sulfides for improved electrocatalytic and supercapacitive performance. *Adv Mater*. <https://doi.org/10.1002/adma.201606814>
- You B, Sun Y (2018) Innovative strategies for electrocatalytic water splitting. *Acc Chem Res* 51:1571–1580. <https://doi.org/10.1021/acs.accounts.8b00002>
- You B, Tang MT, Tsai C, Abild-Pedersen F, Zheng X, Li H (2019) Enhancing electrocatalytic water splitting by strain engineering. *Adv Mater* 31:e1807001. <https://doi.org/10.1002/adma.201807001>
- Yu W, Sun X, Xiao M, Hou T, Liu X, Zheng B, Yu H, Zhang M, Huang Y, Hao X (2021) Recent advances on interface engineering of perovskite solar cells. *Nano Res* 15:85–103. <https://doi.org/10.1007/s12274-021-3488-7>
- Zhang Z, Zhang X, Chen W, Rasim Y, Salman W, Pan H, Yuan Y, Wang C (2016) A high-efficiency energy regenerative shock absorber using supercapacitors for renewable energy applications in range extended electric vehicle. *Appl Energy* 178:177–188. <https://doi.org/10.1016/j.apenergy.2016.06.054>
- Zhang D, Cao J, Zhang X, Insin N, Liu R, Qin J (2020) NiMn layered double hydroxide nanosheets in-situ anchored on Ti₃C₂ MXene via chemical bonds for superior supercapacitors. *ACS Appl Energy Mater* 3:5949–5964. <https://doi.org/10.1021/acsaem.0c00863>
- Zhang W, Fan H, Liu Q, Ta N, Pu Y, Chen X, Sui Y, Wang E, Cao P (2021) Nickel-rich NiCo LDHs supported on hollow carbon shells for hybrid supercapacitors. *Electrochim Acta*. <https://doi.org/10.1016/j.electacta.2021.139167>
- Zhao J, He Y, Chen Z, Zheng X, Han X, Rao D, Zhong C, Hu W, Deng Y (2019) Engineering the surface metal active sites of nickel cobalt oxide nanoplates toward enhanced oxygen electrocatalysis for Zn–air battery. *ACS Appl Mater Interfaces* 11:4915–4921. <https://doi.org/10.1021/acsami.8b16473>
- Zhou B, Zhang M, He W, Wang H, Jian M, Zhang Y (2019) Blue rose-inspired approach towards highly graphitic carbons for efficient electrocatalytic water splitting. *Carbon* 150:21–26. <https://doi.org/10.1016/j.carbon.2019.05.009>
- Zhu J, Sun M, Liu S, Liu X, Hu K, Wang L (2019a) Study of active sites on Se-MnS/NiS heterojunctions as highly efficient bifunctional electrocatalysts for overall water splitting. *J Mater Chem A* 7:26975–26983. <https://doi.org/10.1039/c9ta10860b>
- Zhu Q, Zhao D, Cheng M, Zhou J, Owusu KA, Mai L, Yu Y (2019b) A new view of supercapacitors: integrated supercapacitors. *Adv Energy Mater*. <https://doi.org/10.1002/aenm.201901081>
- Zhu J, Wei P, Zeng Q, Wang G, Wu K, Ma S, Shen PK, Wu XL (2020) MnS@N, S co-doped carbon core/shell nanocubes: sulfur-bridged bonds enhanced Na-storage properties revealed by in situ Raman spectroscopy and transmission electron microscopy. *Small* 16:e2003001. <https://doi.org/10.1002/smll.202003001>
- Zhu Z, Xiang H, Zeng Y, Zhu J, Cao X, Wang N, Wang ZL (2022) Continuously harvesting energy from water and wind by pulsed triboelectric nanogenerator for self-powered seawater electrolysis. *Nano Energy*. <https://doi.org/10.1016/j.nanoen.2021.106776>

Submit your manuscript to a SpringerOpen[®] journal and benefit from:

- Convenient online submission
- Rigorous peer review
- Open access: articles freely available online
- High visibility within the field
- Retaining the copyright to your article

Submit your next manuscript at ► [springeropen.com](https://www.springeropen.com)